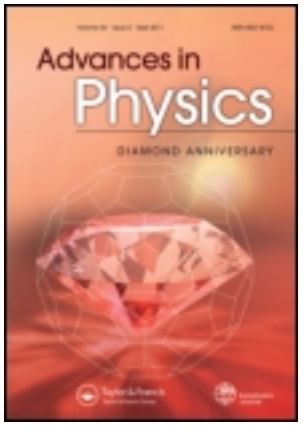

Advances in Physics
Publication details, including instructions for authors and subscription information:
http://www.tandfonline.com/loi/tadp20

Raman spectroscopy of graphene and carbon nanotubes

R. Saito [a], M. Hofmann [b], G. Dresselhaus [c], A. Jorio [d] & M. S. Dresselhaus [b e]

[a] Department of Physics, Tohoku University, Sendai, 980-8578, Japan

[b] Department of Electrical Engineering and Computer Science, Massachusetts Institute of Technology, Cambridge, MA, 02139-4307, USA

[c] Francis Bitter Magnet Laboratory, Massachusetts Institute of Technology, Cambridge, MA, 02139-4307, USA

[d] Departamento de Física, Universidade Federal de Minas Gerais, Belo Horizonte, MG, 30123-970, Brazil

[e] Department of Physics, Massachusetts Institute of Technology, Cambridge, MA, 02139-4307, USA

Available online: 01 Jul 2011

To cite this article: R. Saito, M. Hofmann, G. Dresselhaus, A. Jorio & M. S. Dresselhaus (2011): Raman spectroscopy of graphene and carbon nanotubes, Advances in Physics, 60:3, 413-550

To link to this article: http://dx.doi.org/10.1080/00018732.2011.582251

Advances in Physics
Vol. 60, No. 3, May–June 2011, 413–550

Taylor & Francis
Taylor & Francis Group

REVIEW ARTICLE

Raman spectroscopy of graphene and carbon nanotubes

R. Saito[a], M. Hofmann[b], G. Dresselhaus[c], A. Jorio[d], and M.S. Dresselhaus[b,e]*

[a]*Department of Physics, Tohoku University, Sendai 980-8578, Japan;* [b]*Department of Electrical Engineering and Computer Science, Massachusetts Institute of Technology, Cambridge, MA 02139-4307, USA;* [c]*Francis Bitter Magnet Laboratory, Massachusetts Institute of Technology, Cambridge, MA 02139-4307, USA;* [d]*Departamento de Física, Universidade Federal de Minas Gerais, Belo Horizonte - MG, 30123-970, Brazil;* [e]*Department of Physics, Massachusetts Institute of Technology, Cambridge, MA 02139-4307, USA*

(*Received 28 June 2010; final version received 5 April 2011*)

This paper reviews progress that has been made in the use of Raman spectroscopy to study graphene and carbon nanotubes. These are two nanostructured forms of sp^2 carbon materials that are of major current interest. These nanostructured materials have attracted particular attention because of their simplicity, small physical size and the exciting new science they have introduced. This review focuses on each of these materials systems individually and comparatively as prototype examples of nanostructured materials. In particular, this paper discusses the power of Raman spectroscopy as a probe and a characterization tool for sp^2 carbon materials, with particular emphasis given to the field of photophysics. Some coverage is also given to the close relatives of these sp^2 carbon materials, namely graphite, a three-dimensional (3D) material based on the AB stacking of individual graphene layers, and carbon nanoribbons, which are one-dimensional (1D) planar structures, where the width of the ribbon is on the nanometer length scale. Carbon nanoribbons differ from carbon nanotubes is that nanoribbons have edges, whereas nanotubes have terminations only at their two ends.

PACS: 78.30.-j Raman Spectroscopy; 61.48.Gh Structure of graphene; 61.48.De Structure of nanotubes; 71.38.-k Polarons and electron-phonon interactions.

Keywords: resonance Raman spectroscopy; carbon nanotubes; graphene nanoribbons; electron–phonon interaction

Contents PAGE

*Corresponding author. Email: millie@mgm.mit.edu

ISSN 0001-8732 print/ISSN 1460-6976 online

DOI: 10.1080/00018732.2011.582251
http://www.informaworld.com

This review of the Raman spectroscopy of graphene and carbon nanotubes starts with a brief presentation of background material to set the stage for a discussion of the present status of knowledge on this topic by providing a broad overview of the field in Section 1. This is followed, in Section 2, by an overview discussion of experimental progress that has been made in recent years using many experimental techniques. Advances in the theoretical understanding needed to interpret the many new results that appear daily on the photo-physics of graphene and carbon nanotubes are reviewed in Section 3. The detailed consideration of the Raman spectroscopy of graphene and carbon nanotubes is presented in Sections 4 and 5, both individually and comparatively, while Section 6 looks at future developments in this field. A textbook helpful for understanding background material relevant to this review article has recently been published [1].

Hereafter in, Section 1, we provide background to Raman spectroscopy in general, giving special attention to resonance Raman spectroscopy, with illustrations of the various photo-physical phenomena, which are given in terms of graphene and carbon nanotubes. Raman measurements in low-dimensional (one- and two-dimensional) systems are then discussed in general terms, giving specific examples of the differences and similarities between the Raman spectra for graphene and carbon nanotubes in relation to other sp^2 carbons. Finally, we discuss what can be learned from the Raman spectrum from one laser line in comparison to what can be learned from using a continuum of laser lines.

1. Basic concepts

In this section, we introduce the basic concepts of Raman spectroscopy, starting with where they stand within the broad picture of light–matter interactions and then considering their general characteristics. The concepts of first-order and higher-order scattering processes, Stokes vs. anti-Stokes processes, lineshapes, resonance and coherent processes are introduced, as well as the classical treatment of the Raman effect. Subsequently, we present a historical description of the Raman spectroscopy used to study and characterize graphitic materials, from graphite to single-walled carbon nanotubes (SWNTs) and graphene. This brief introduction to the Raman spectroscopy of sp^2 nanocarbons should be useful to general readers who may not be so familiar with Raman spectroscopy.

1.1. *Overview of sp^2 carbon materials*

We start this section with a brief history of several important carbon materials.

1.1.1. *Graphite*

Carbon materials have been the objects of study and use for many years [2]. Three-dimensional (3D) graphite is one of the longest known forms of pure carbon, naturally occurring on the surface of the earth as a mineral (as, for example, in the mineral deposits of Ticonderoga (New York) graphite, Ceylon (Sri Lanka) and the large graphite deposits in Minas Gerais, Brazil). Structurally, graphite is a layered material, with individual graphene layers, as shown in Figures 1 and 2(a). These individual graphene layers are stacked in the ABAB Bernal stacking order in the most common form of graphite, as shown in Figure 2(b) to illustrate the relative in-plane atomic arrangements of the A and B carbon atoms within the layer plane and in adjacent layers. Here, one type of carbon atom (labeled A) is aligned on top of another A atom in the direction perpendicular to the graphene layer, while the other type (the B carbon atom) is aligned in every other layer[1] [2], so that the graphene planes are arranged in the so-called ABAB Bernal stacking sequence, as shown in Figure 2(c) [6], where a carbon atom is found on adjacent layer planes over the empty center of a hexagon. This AB stacking order (Figure 2(c)) also applies to bi-layer graphene prepared by the

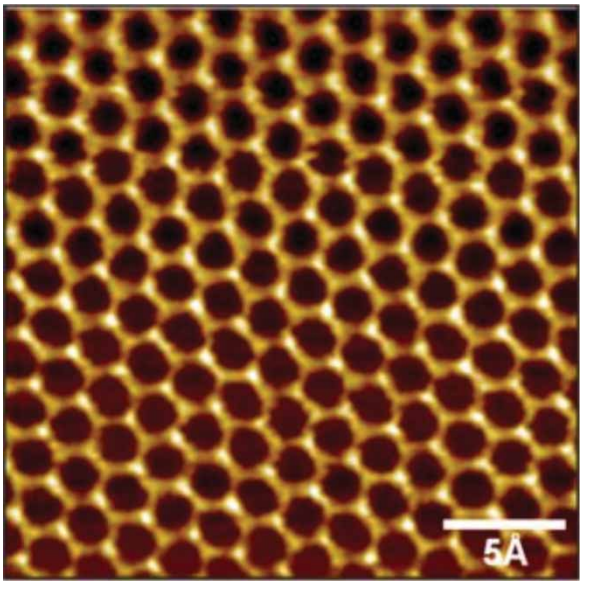

Figure 1. STM image of graphite. Notice the different brightness for the A and B atoms (see footnote 1). Reprinted from Carbon, 48(5), M.M. Lucchese *et al.* pp. 1592–1597 [3]. Copyright © (2010) Elsevier.

mechanical exfoliation method [7,8], while Figure 2(d) shows the stacking arrangement of trilayer graphene. In graphite, layers 1 and 3 are crystallographically equivalent and are translated from one another by the out-of-plane lattice parameter $c = 0.670$ nm (see Figure 2(d)), thus generating hexagonal graphite. Another related crystalline arrangement is the less common form known as rhombohedral graphite [9], which has an ABC stacking order, consisting of three layers and a lattice constant of 1.005 nm.

Of all materials, graphite has the highest melting point (4200 K), the highest thermal conductivity (3000 W/mK) and a high room-temperature electron mobility (30, 000 $cm^2/V\,s$) [10,11]. 3D graphite was synthesized for the first time in 1960 by Arthur Moore and co-workers [12–16] and their high-temperature, high-pressure synthesis method yielded the material commonly known as highly oriented pyrolytic graphite (HOPG). Graphite and its related carbon fibers [17–19] have been used commercially for decades [20]. Carbon fiber applications range from use as conductive fillers, and as mechanical structural reinforcements in composites (e.g., in the aerospace industry), to their use as electrode materials for making steel, exploiting their good electrical conductivity and in lithium ion battery applications exploiting their high resiliency [20,21].

1.1.2. *Fullerenes*

In 1985, the discovery of another unique sp^2 carbon system took place, the observation of the C_{60} fullerene molecule [22]. The fullerene molecule consists of 60 carbon atoms with mostly sp^2 bonding and appropriate π bonding to form a closed surface with full icosahedral symmetry. Because of topological restrictions, fullerenes, in general, have 12 pentagonal rings and any numbers of hexagonal rings, thereby generating a large variety of C_n fullerene molecules. The C_{60} molecule with full icosahedral symmetry can be regarded as the first isolated carbon nanosystem. Fullerenes stimulated and motivated a large scientific community into new research directions from the time of their discovery up to the end of the twentieth century, but fullerene-based applications

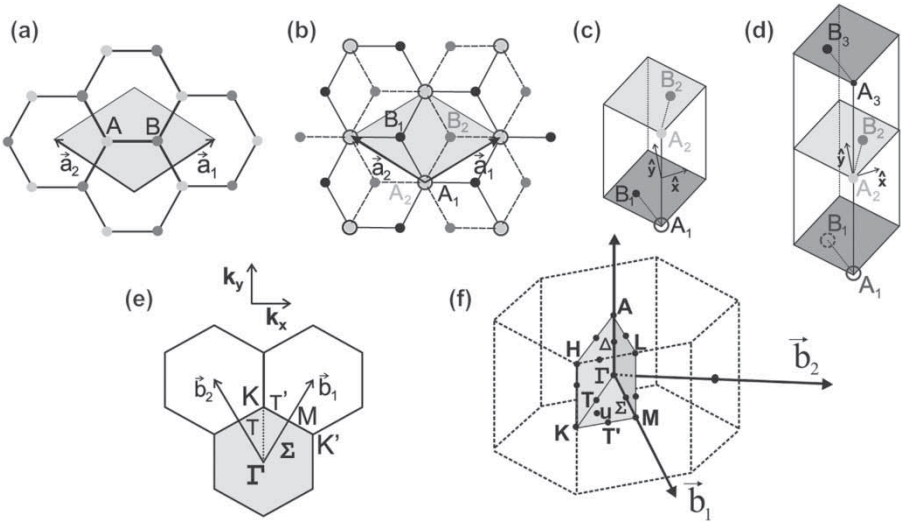

Figure 2. (a) Top view of the real space unit cell of mono-layer graphene showing the inequivalent carbon atoms A and B and the graphene unit vectors $\mathbf{a}_1$ and $\mathbf{a}_2$. (b) Top view of the real space bi-layer graphene structure. The light/dark gray dots and black circles/black dots represent the carbon atoms in the upper and lower layers, respectively, of bi-layer graphene (2-LG). (c) The unit cell and the *x* and *y* unit vectors of bi-layer graphene and (d) the same as (c) but for trilayer graphene. (e) The reciprocal space unit cell showing the first Brillouin zone with its high symmetry points and lines, such as the line *T* connecting Γ to *K*. (f) The Brillouin zone for 3D graphite showing high symmetry points and axes. Here Δ is a high symmetry point along the axis connecting points *A* and Γ, and *u* is a general point in the *KM*Γ plane. Adapted figure with permission from A. Jorio *et al.* Spectroscopy in Graphene Related System, 2010 [1] Copyright © Wiley-VCH Verlag GmbH & Co. KGaA; and with permission from L. M. Malard *et al.*, Physical Review B 79, p. 125426, 2009 [4]. Copyright © (2009) by the American Physical Society; and with permission from Physics Reports 473, L.M. Malard *et al.* pp. 51–87 [5]. Copyright © (2009) Elsevier.

remain sparse to date. In this review, we do not mention fullerenes much. See [23] for more information on fullerenes.

1.1.3. *Carbon nanotubes*

Carbon nanotubes arrived actively on the scene in 1991 following the footsteps of the emergence of the C_{60} fullerene molecule. Since their emergence, carbon nanotubes have evolved into one of the most intensively studied materials, now being held responsible for co-triggering the nanotechnology revolution. The strong entry of nanotubes on the scene in 1991 was through a report of the observation of multi-walled carbon nanotubes (MWNTs) on the cathode of a carbon arc used to produce fullerenes [24]. Actually, carbon nanotubes had been identified in the 1970s in the core structure of vapor-grown carbon fibers as very small carbon filaments [25–27] and carbon fibers were reported even earlier in the 1950s in the Russian literature [28] (see Figure 3). However, single-walled carbon nanotubes (SWNTs), the most widely studied carbon nanostructure in the 1995–2005 timeframe, were first synthesized systematically in 1993 [30,31]. Carbon nanotube research took off at this point in time. The great interest in the fundamental properties of carbon nanotubes and in their exploitation through a wide range of applications is due to their unique structural, chemical, mechanical, thermal, optical, optoelectronic and electronic properties [21,32,33]. The growth of an SWNT at a specific location and point in a given direction and the growth of a huge

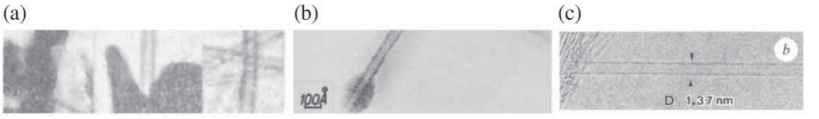

Figure 3. Early transmission electron microscopy images of carbon nanotubes [29]. The early reported observations of nanotubes (a) in 1952 [28] and (b) in 1976 [25]. (c) Observation of SWNTs that launched the field in 1993 [30,31] together with an example of their observation. Adapted figure with permission from Carbon 14(2), A. Oberlin *et al.*, pp. 133–135 [25]. Copyright © (1976) Elsevier; and with permission from Carbon 44, M. Monthioux and V.L. Kuznetsov, pp. 1621–1623 [29]. Copyright © (2006) Elsevier; and with permission from Macmillan Publishes Ltd. Nature [30]. Copyright © (1993); and with permission from Macmillan Publishes Ltd. Nature [31], Copyright © (1993).

amount of millimeter-long nanotubes with nearly 100% SWNT purity (absence of other carbon forms) have now been achieved [34], and further improvements in nanotube synthesis are evolving rapidly at this time. Substantial success with the separation of nanotubes by their (n, m) structural indices, metallicity (semiconducting or metallic) and by their length has been achieved by different methods, especially by the density gradient approach of Hersam and Arnold [35]. Advances have been made with doping either n-type or p-type nanotubes for the modification of their properties, as summarized in reference [36,37]. Studies on nanotube mechanical properties [37,38], optical properties [39–45], magnetic field-dependent properties [46], optoelectronics [47,48], transport properties [49] and electrochemistry [50,51] have exploded, revealing many rich and complex fundamental excitonic and other collective phenomena [21]. Nanotube-based quantum transport phenomena, including quantum information applications, spintronics and superconducting effects, have also been explored [49]. After more than a decade and a half of intense activity in carbon nanotube research, more and more attention is now being focussed on the practical applications of the many unique and special properties of carbon nanotubes [20]. Further background information on the synthesis, structure, properties and applications of carbon nanotubes can be found in [1,21] and some of these topics are further emphasized in the present review.

1.1.4. *Graphene*

The interest in a single atomic layer of sp^2 carbon (called graphene; see Figure 1) goes back to the pioneering theoretical work of Wallace in 1947 [52] which was for many years used as a model system for all sp^2 carbons. This very early work provides a framework for comparing the structures of graphite, fullerenes, carbon nanotubes and other sp^2 nanocarbons. The synthesis of single-layer graphene was actually reported by Boehm in 1962 [53], but this early discovery was neither confirmed nor followed up for many years.

More recently, mono-layer graphene was synthesized from nano-diamonds in 2001 [54] and from SiC [55]. The material synthesized from nano-diamonds is generally a few-layer graphene material but thin ribbon specimens of mono-layer thickness are also contained in such samples. In the studies on these nanoribbons, emphasis was given to the properties of edges of the nanoribbons and especially to the magnetic properties of these edges [54,56–59]. The graphene prepared from heating SiC to 1300 °C emphasized the 2D electron gas properties of this graphene in an electric field, but did not especially focus on the number of layers [55].

The widespread study of graphene was launched by the preparation of mono-layer graphene by Novoselov *et al.* [7], using a simple Scotch tape method to prepare and transfer mono-layer graphene from the *c*-face of graphite to a suitable substrate such as SiO_2 for the measurement of the electrical and optical properties of mono-layer graphene [60]. The Novoselov and Geim studies of transport in few-layer graphene in 2004 [7] led to a renewed interest in mono-layer and

few-layer graphene and to an in-depth study of the unique properties of this material in the mono-layer and bi-layer limit. Surprisingly, this very basic system, which had been conceptually utilized by researchers over a period of many decades, suddenly appeared on the experimental scene, demonstrating many novel physical properties that were not even imagined previously [60,61]. The discovery of these novel properties launched a rush into the study of graphene science in the first decade of the twenty-first century, and culminating in the 2010 Nobel Prize in physics [62].

Besides the outstanding mechanical properties [63] (breaking strength $\sim$40 N/m, Young's modulus $\sim$1.0 TPa) and thermal properties [64,65] (room temperature thermal conductivity $\sim$3000 W m^{-1} K^{-1} [65]), the scientific interest in graphene was stimulated [66,67] by the widespread report of the relativistic (massless) electronic properties of the conduction electrons (and holes) in a single layer less than 1 nm thick, with a state-of-the-art mobility reaching $\mu = 200,000\,\mathrm{cm}^2/\mathrm{V\,s}$ at room temperature for freely suspended graphene [66–71]. Other unusual properties have been predicted and demonstrated experimentally, such as the minimum conductivity and the half-integer quantum Hall effect in mono-layer graphene [72] and the integer quantum Hall effect in bi-layer graphene [73], ambipolar transport by either electrons or holes by the variation of a gate potential, operation as a transparent conductor [47,74], Klein tunneling [75–82], negative refractive index and Veselago lensing [80], anomalous Andreev reflections at metal–superconductor junctions [76,81–84], anisotropies under antidot lattices [85] or periodic potentials [86], and a metal–insulator transition via hydrogenation of graphene [87]. Applications such as fillers for composite materials, as super-capacitors, batteries, interconnects and field emitters are being developed, although it is still too early to say to what extent graphene will be able to compete with carbon nanotubes and other established materials systems in the applications world [88]. Although nanotubes and graphene are both carbon-based nanostructures, they have different properties related to the planar aspects of graphene and the tubular aspects of nanotubes, and this basic difference should distinguish their optimal usage in applications.

1.1.5. *Nanoribbons*

Graphene nanoribbons are of particular interest for introducing a bandgap into graphene-related systems. Bandgaps are needed for many electronics applications of nanomaterials. Since graphene can be patterned using, for example, high-resolution lithography [55,89], nanocircuits with graphene–nanoribbon interconnects can be fabricated. Many groups are now fabricating devices using graphene and also graphene nanoribbons, which have a long length and a small nanoscale width, and where the ribbon edges play an important role in both determining their electronic structure and exhibiting unusual spin polarization properties [56]. Nanoribbons of small widths exhibit 1D behavior analogous to carbon nanotubes, but have a high density of electronic states at the Fermi level for the case of well-defined zigzag edges. This high density of electronic states allows us to experimentally distinguish zigzag nanoribbons from armchair and chiral nanoribbons which do not exhibit this property. While lithographic techniques have limited resolution for the fabrication of small width nanoribbons ($<$20 nm wide), chemical [90] and synthetic [91] methods have been employed successfully, including the unzipping of SWNTs as a route to produce carbon nanoribbons [92,93]. Carbon nanoribbons have been shown to be especially sensitive for the study of edge structures and edge properties and edge reconstruction effects [94].

1.1.6. *Raman spectroscopy for sp^2 carbon materials*

Raman spectroscopy is the inelastic scattering of light, usually associated with the emission (Stokes process) or absorption (anti-Stokes process) of phonons [95]. By knowing the energy shift of the scattered light relative to the incident light, which yields Raman spectra in cm^{-1} (see Figure 4),

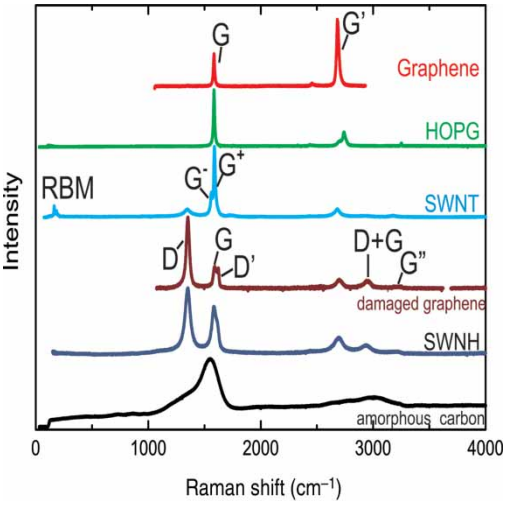

Figure 4. Raman spectra from several sp^2 nanocarbon and bulk carbon materials. From top to bottom: crystalline mono-layer graphene, HOPG, an SWNT bundle sample, damaged graphene, single-wall carbon nanohorns (SWNH). The most intense Raman peaks are labeled in a few of the spectra [1,96]. Note that some authors call the G' by 2D and the G" by 2D' [97]. Reprinted with permission from M.S. Dresselhaus *et al.*, Nano Letters 10, pp. 953–973, 2010 [96]. Copyright © (2010) American Chemical Society.

we can obtain the phonon frequency which is useful for identifying the origin of an unknown structure of a newly discovered molecule or of a new material in chemistry [98]. Among all possible phonon modes for sp^2 carbons, only a limited number of phonons are Raman-active modes (namely those with A, E_1 and E_2 symmetry for carbon nanotubes, and E_{2g} for graphite) [99–101]. A common metric used to characterize the defect density in a material is the ratio of the intensities of the disorder-induced D-band to the symmetry-allowed G-band ratio (I_D/I_G) [102]. Study of the D- and G-band modes by Raman spectroscopy (see Figure 4) yields information about the crystal structure of the material and about many of its interesting physical properties.

Raman spectroscopy for the various sp^2 carbon materials (see Figure 4) has been mainly used for sample characterization and these different carbon materials exhibit characteristic differences related to the small differences in their structures. The fundamental sp^2 carbon material is mono-layer graphene which has the simplest and most fundamental spectrum showing the two Raman-allowed features that appear in all sp^2 carbon materials – the first-order G-band and the second-order symmetry-allowed G′-band,[2] where the symbol G is used to denote "graphitic." The next most commonly observed feature is the D-band that is a defect-activated Raman mode. The D-band occurs at about 1350 cm^{-1} at 2.41 eV laser excitation energy (E_{laser}) and is highly dispersive as a function of E_{laser} (see Section 2.8.9). Since the graphite melting temperature is very high (over 4200 K) and since no actual carbon materials are defect-free, the D/G-band intensity ratio (I_D/I_G) provides a sensitive metric for the degree of disorder in sp^2 carbon materials over a wide temperature range. In the case of fullerenes, a special Raman-active phonon mode related to the vibrations of a pentagonal ring (1469 cm^{-1}) is particularly sensitive for understanding the molecular structure [23]. In the case of carbon nanotubes, it is common to survey unknown samples using Raman spectroscopy to check for the presence of nanotubes in the sample by observing the cylindrical-specific, Raman-active-mode radial breathing mode (RBM) in which atoms around the circumference of a single wall carbon nanotube (SWNT) are vibrating in a breathing mode in the radial direction (see Figure 4) [32,100,103–110]. This vibrational mode is unique to carbon nanotubes and serves to sensitively identify their presence in a given sample. Since the RBM frequency

ω_{RBM} is inversely proportional to the nanotube diameter d_t, we can thus estimate the diameter distribution of the nanotubes that are contained in a given sample [111]. When we observe an isolated nanotube, we can use its Raman spectrum to obtain its detailed structure, which involves identification of the spatial orientation, the diameter and the chiral angle of the nanotube, as well as the nanotube (n, m) chirality assignment. This (n, m) assignment is based on the concept of the resonance Raman effect (see Section 1.5.2). In the case of graphene [112–114], the intensity ratio $(I_{\mathrm{G}'}/I_{\mathrm{G}})$ and the lineshape of the G′-band (along with other indicators) can be used for identifying the number of graphene layers (see Section 4.2.1). For graphene ribbons, we can use Raman spectroscopy to study the edge structure of the ribbons [94,115] to yield information about the structure and properties of graphene ribbons (see Section 4.4). For all these reasons, Raman spectroscopy is very sensitive for the characterization of sp^2 carbons.

Since most carbon materials are not soluble in water, Raman spectroscopy is useful as an *in situ*, non-contact, non-destructive measurement tool that can be used at room temperature and under ambient operating conditions, as well as for freely suspended carbon nanotubes and graphene samples. Combining the continuing advances in optical techniques with new theoretical developments that are rapidly developing, Raman spectroscopy studies of graphene and carbon nanotubes have provided a great deal of information about their solid-state properties, which are the main subjects of this review, including their behavior as a function of temperature, pressure and Fermi energy [1].

1.2. *Various photo-physical processes*

In this section, various optical processes that are useful for the characterization of nanostructures are very briefly discussed. The Raman effect [116,117] is briefly mentioned in this section, but is further discussed in Sections 1.4–1.5.

When focusing light into a material (molecule or solid), part of the energy just passes through the sample (by transmission), while the remaining photons interact with the system through light absorption, reflection, light emission or light scattering. The amount of light that will be transmitted, as well as the details for all the light–matter interactions, are determined by the electronic and vibrational properties of the material. Furthermore, different phenomena occur when focusing light with different energy photons into a given material [95,118], because different photon energies will be related to the different optical transitions occurring in the medium. As an example of the richness of light–matter interactions, an overview of various optical absorption mechanisms for a semiconducting material is shown in Figure 5. Using this figure as a guide, examples are given for the many different effects that might occur when light interacts with a material. Starting from the high-energy side of the diagram moving to mechanisms important at lower energies, Figure 5 shows the absorption coefficient as a function of the energy of the photon which yields the absorption spectra and enumerates the dominant photo-physical processes that are involved in the various photon energy regimes in Figure 5 [95].

1.2.1. *Valence-to-conduction band transitions and excitons*

A photon (having an energy in the 1–5 eV range) can be absorbed by an electron making a transition from the valence band to the conduction band, as shown in Figure 5. Such a transition generates a free electron in the conduction band, leaving behind a "hole" in the valence band, where we use the nomenclature for electrons and holes as used in semiconductor physics [119].

Photons with an energy smaller than the energy gap can generate a transition to an exciton level, thereby creating an exciton which corresponds to an electron bound to a hole through the Coulomb interaction. Although excitonic levels in model semiconducting systems such as GaAs

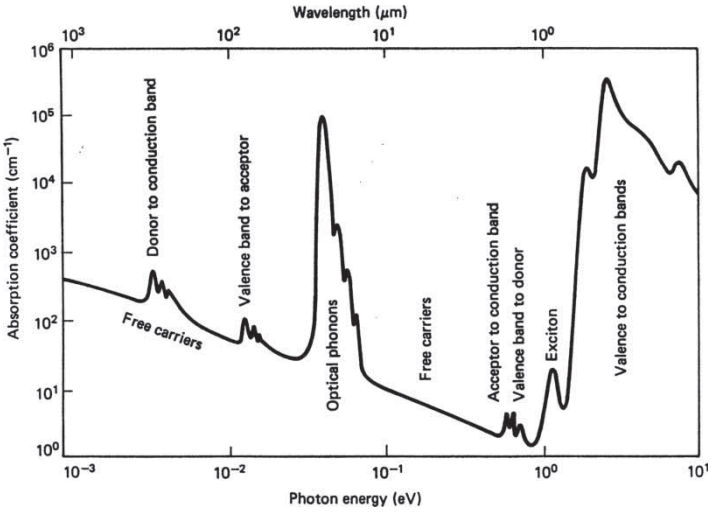

Figure 5. Photo-physical mechanisms operative for various regions of the electromagnetic spectrum as photons in various energy ranges interact with materials. Reprinted figure with permission from A. Jorio *et al.* Spectroscopy in Graphene Related Systems, 2010 [1]. Copyright © Wiley-VCH Verlag GmbH & Co. KGaA.

have excitonic levels of a few meV below the bandgap, the excitonic levels in carbon nanotubes are much larger (on the order of a few hundred meV), emphasizing the greater importance of excitonic effects in low-dimensional nanosystems. Optical absorption in the case of carbon nanotubes was predicted by Ando to be excitonic as far back as 1997 [120] and the importance of excitons in nanotubes was demonstrated experimentally by the two photon experiments carried out by the Heinz group in 2005 [121] and a similar result was independently obtained by the Berlin group [122]. These experiments confirm theoretical concepts that excitonic effects would be enhanced in low-dimensional systems. Although excitonic effects were found to be much larger in semiconducting nanotubes than in metallic nanotubes, excitons nevertheless have been found in these works to also dominate optical absorption processes in metallic nanotubes.

1.2.2. *Optical transitions including impurity levels*

Impurities can form states within the bandgap of semiconducting materials. If the impurity atom has more valence electrons than the atom it replaces, then this impurity will act as an electron donor making the nanotube an n-type semiconductor. However, if the impurity atom has fewer electrons, then it will behave like an electron acceptor giving rise to a p-type semiconductor. Light can be absorbed, generating electronic transitions from the valence band to such donor impurity levels, or optical transitions can be made by taking electrons from an acceptor level to the conduction band of a semiconductor. For semiconducting carbon nanotubes, typical photon energies for these impurity levels are in the 10–100 meV range about a band edge, but they usually occur over an energy range smaller than the energy gap.

Optical transitions to conduction band impurity levels or from valence band shallow acceptor levels can also be responsible for light absorption. The corresponding photon energy would be significantly lower than the stronger excitations from the dominant bright allowed state. In materials, such as carbon nanotubes, the lowest energy transitions however involve dark exciton states, thereby lowering the intensity of these transitions.

1.2.3. *Optical phonons*

Optical absorption by phonons typically occurs when the incident photon energy coincides with the energy of optical phonons, corresponding, in general, to 50 meV to 0.2 eV for first-order processes. These absorption processes generally occur in the infrared energy range and play a major role in the field of infrared spectroscopy for both molecules and solid-state systems.

In sp^2 carbon systems, the harmonics and combination modes of symmetry-allowed optical phonons are clearly observed in the Raman spectra through double resonance (DR) processes. Thus phonon-related effects can be observed over a photon energy range up to ~350 meV for the observation of phonon-related effects. It is noted that Raman processes and infrared absorption processes generally occur at different photon energies because, in general, different phonons are Raman- and infrared-active for high symmetry materials such as sp^2 carbons.

1.2.4. *Free carrier processes*

Free carriers provide another mechanism for optical absorption. Free carriers are dominant in metallic systems and are present in doped semiconducting systems through electrons and/or holes. These carriers can also absorb light, usually occurring over a broad energy range from 1 to 10 meV. Other free carrier processes not shown explicitly in Figure 5 also occur. In a higher energy region (1–10 eV), collective excitations of electrons also occur, giving rise to plasmon absorption. At much higher energies in the ultraviolet and X-ray range, transitions from core levels also take place, generating photo-excited electrons, which can be observed by ultraviolet photo-electron spectroscopy (UPS) and X-ray photo-electron spectroscopy (XPS), depending on the energy of these deeper levels. By measuring the momentum and energy of photo-electrons for a given momentum and energy, information can be obtained about the momentum and energy of the incident electron in the valence energy band, by the angle-resolved photo-emission spectroscopy (ARPES) technique, which has been widely used for observing electron energy dispersion in single layer and multi-layer graphene [123–126].

1.3. *Interactions for optical processes*

In this section, we focus on the different phenomena occurring through light–matter interactions [95] (see Figure 6). The potential energy profile of an atom is modified by the electric field of the incident photon, so that the energy and momentum of the incident light are changed in a scattering process and a resulting photoluminescence or fluorescence process that frequently occurs after absorption by an atom gives important information about this interaction. However, typical times for the occurrence of such photoluminescence or fluorescence processes are much longer (in ns or ms, respectively) than for typical light scattering events (in ps). We now briefly review the various light–matter interactions.

1.3.1. *Photon-induced electron–phonon interaction*

Two kinds of light scattering processes are the elastic and inelastic scattering processes, which are called the Rayleigh and the Raman scattering, respectively. In the case of Rayleigh scattering, only the direction of the light is changed with no change in photon energy, while in the case of Raman scattering, either phonon creation or annihilation occurs in the scattering process. When the electric field associated with the photon interacts with an atom, the electron and the ion core move in opposite directions to each other to form a dipole and this oscillating dipole interacts with the incident photon to generate the scattered light. The coupling of the dipole with the electric field of the photon creates a phonon which is described by an electron phonon

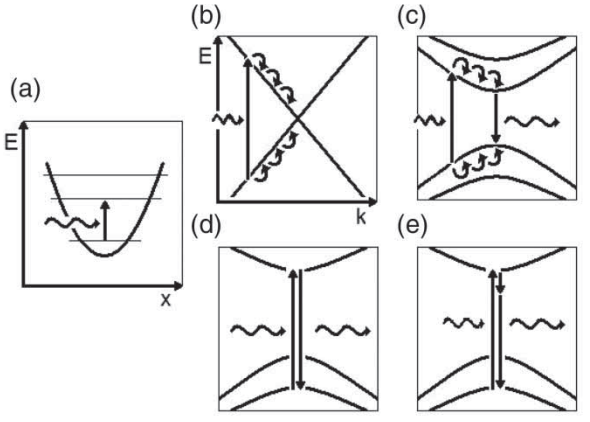

Figure 6. The light–matter interaction, showing the most commonly occurring processes. The waved arrows indicate incident and scattered photons. The vertical arrows denote photon-induced transitions between (a) vibrational levels and (b–e) electronic states. Curved arrow segments indicate electron–phonon (el–ph) (hole–phonon) scattering events. In (e), the shortest vertical arrow also indicates an el–ph transition in Raman scattering. In (d, e), the processes are resonant if the incident (or scattered) photon energy exactly matches the energy difference between initial and excited electronic states. When far from the resonance window where resonance occurs, the optical transition is called a virtual transition. The intensity for resonance Raman scattering can be much larger for vertical processes that are resonant than those that are not resonant [1,95]. Reprinted figure with permission from A. Jorio *et al.* Spectroscopy in Graphene Related Systems, 2010 [1].

(el-ph) interaction that occurs in the Raman scattering process. In this process the electron is excited to a virtual state, for which the stable geometry of the chemical bond is no longer identical to that of the ground state. This perturbation generates a force resulting in atomic motion, thereby providing a quantum explanation for the el–ph interaction. If the incident photons are introduced through a sufficiently short light pulse with a duration comparable to the frequency of the phonon, then all atoms start to move at the same time as a result of the el–ph interaction, thereby creating a coherent motion of the atoms which can be detected by a second pulse of light at a frequency at which the material is transparent. This sensitive technique is known as coherent phonon spectroscopy.

1.3.2. *Electron–phonon interaction in infrared absorption*

When the photon energy matches the energy for allowed phonon creation, the photon can transfer energy directly to create an acoustic or optical phonon (see Figure 6(a)). This resonance process is called infrared (IR) absorption, since the phonons that are created have energies corresponding to IR photon frequencies. IR-active phonon modes are phonon modes that have the symmetry of a vector [1], which describes the vibration of an oscillating dipole moment of the ions in the material. The dipole moment is directly coupled to the electric field associated with the incident and scattered photons. We describe this interaction by an electromagnetic interaction perturbation Hamiltonian between the vibrating atoms and the photons that induce the vibration. Since all the atoms in nanocarbon materials are neutral carbon atoms, the dipole moment for IR absorption is generated by photo-excited electrons created by the optical electric field.

1.3.3. *Dipole–phonon interaction in non-radiative decay*

For higher photon energies, the photons are absorbed by exciting an electron–hole (e–h) pair, as shown in Figure 6(b). The photo-excited electron (or hole) then loses energy to electrons in the

bottom (top) of the conduction (valence) energy band by creating multiple phonons of different frequencies through el–ph coupling, in which the phonons are selected such that the initial and final electronic states satisfy both energy and momentum conservation requirements. In the case of a metal, such photo-excited electrons (together with their holes) will decay down (up) to the ground states without emitting a photon, and such processes are called non-radiative decay process as shown in Figure 6(b). In graphene or metallic carbon nanotubes, non-radiative decay that generates heat frequently occurs and can have a special character because of their linear $E(k)$ dispersion relation.

1.3.4. *Dipole–photon interaction in photoluminescence*

If the material has an energy gap between the occupied (valence) and unoccupied (conduction) bands, the photo-excited electron quickly (on a ps timescale) decays to the bottom of the conduction band by an el–ph process and then to its ground state by emitting a photon with the bandgap energy on a ns timescale, in a light emission process (see Figure 6(c)). This emission process is called photoluminescence, and the energy decrease from the incident photon to the scattered photon is generally called a Stokes process because of the decreased energy of the emitted photon.[3] In order to get photoluminescence emission, an interaction between the dipole moment of the atom with the electric field of the photon is essential in which the dipole-selection rule must be satisfied for the electronic excited states. When the energy gap is smaller than the optical phonon energy, no photoluminescence occurs, but phonon emission can occur by an inter-band el–ph interaction. In this case, the quantum efficiency for photon generation by the photo-excited electrons is suppressed significantly.

1.3.5. *Rayleigh scattering*

In the Rayleigh scattering process, a photon is virtually[4] absorbed by a material and the oscillating electric field of the photon just shakes the electrons. In this case, the electrons just scatter that energy back to another photon having the same energy as the incident photon. When the incident and scattered photons have the same energy, the scattering process is said to be "elastic" and is named Rayleigh scattering (see Figure 6(d)). Elastic scattering occurs by an interaction of the electric field of the photons with the crystal or atomic potential and it can occur even for the case of real absorption, in which the Rayleigh scattering intensity is enhanced significantly, and such a process is called the resonance Rayleigh scattering [44].

1.3.6. *Brillouin scattering*

In solid materials, a further distinction is made between the inelastic scattering by acoustic phonons (called Brillouin scattering) and by optical phonons (called Raman scattering). Brillouin scattering occurs by an el–ph interaction with acoustic phonons or with any other low-energy excitation such as a magnon. The concept of Brillouin scattering does not apply to molecular systems for which the acoustic phonon would represent a translation of the molecule. Since Brillouin scattering generally appears in a lower energy region than that for an optical phonon, a special experimental set-up based on low-frequency instrumentation is required for observing Brillouin scattering, namely a set-up that very strongly suppresses the presence of the Rayleigh signal. When the Brillouin scattering is stimulated by the electric field of the laser light itself, a strong Brillouin signal is obtained which is known as stimulated Brillouin scattering.

1.3.7. *Raman scattering*

The inelastic scattering of light is called the Raman effect, named in honor of the discoverer of the Raman effect in 1927, commonly attributed to Sir Chandrasekhara Venkata Raman (1888–1970),

an Indian scientist who was awarded the Nobel Prize in Physics in 1930 for his work on "the scattering of light and for the discovery of the effect named after him". In the Raman process, an incident photon with energy $E_i = E_{laser}$ and momentum $k_i = k_{laser}$ reaches the sample and is scattered, resulting in a photon with a different energy E_s and a different momentum k_s. For energy and momentum conservation,

$$E_s = E_i \pm E_q \quad \text{and} \quad k_s = k_i \pm q, \tag{1}$$

where E_q and q are the energy and momentum change during the scattering event induced by electromagnetic excitation of the medium. The quantities E_q and q can be considered to be the energy and the momentum of the phonon.

The Raman process which emits (absorbs) a phonon is called a first-order Raman process. In order to recombine an electron at k_s with a hole at k_i, the wavevector q should be almost zero. Thus, only phonons near the Γ point (zone-centered phonon) in the phonon dispersion relation can be Raman-active modes. However, when we consider second-order Raman processes in which two scattering events are involved, the restriction for $q = 0$ is relaxed. Further, the photo-excited electrons in sp^2 carbons are located in k space near the hexagonal corners of the 2D Brillouin zone (BZ), named the K and K' points, where the states of lowest energy are located. Here, there are two possibilities for $q \neq 0$ scattering: intra-valley ($K \to K$, $K' \to K'$) and inter-valley scattering ($K \to K'$, $K' \to K$). We will show (see Section 2.8.4) that a double resonance Raman process involving excitations near the K and K' points in the 2D BZ yields a large Raman signal.

1.3.8. *First- and higher-order Raman processes*

The order of the Raman process is given by the number of scattering events that are involved in the Raman process. The most usual case is the first-order Stokes Raman scattering process, where the photon energy excitation creates one phonon in the crystal with a very small momentum ($q \approx 0$). If two, three or more scattering events occur in the Raman process, then the process is called second-, third-, or higher-order, respectively. The first-order Raman process gives the basic quantum of vibration, while higher-order processes give very interesting information about overtones and combination modes. In the case of overtones, the Raman signal appears at nE_q ($n = 2, 3, \ldots$) and the Raman signal from combination modes appears at the sum of the different phonon energies ($E_{q1} + E_{q2}$, etc). An interesting point in the higher-order Raman signal in a solid material is that the restriction for $q \approx 0$ in a first-order Raman scattering process is relaxed. The photo-excited electron at k can be scattered to $k + q$ and can go back to its original position at k after the second scattering event by scattering a phonon with wavevector $-q$, which allows the recombination of the photo-excited electrons with their corresponding holes. The probability for selecting a pair of q and $-q$ phonons is usually small and not very important for solids. However, we see in Section 2.8.4–2.8.10 that, under special resonance conditions (the DR condition) commonly occurring in sp^2 nanocarbons, we can expect a clear Raman signal from $q \neq 0$ scattering events.

1.4. *Characteristics of the Raman effect*

Next, we very briefly define in this section a number of the important characteristics of the Raman effect that will be commonly used throughout this article. We first discuss the Raman spectra giving special emphasis to low-dimensional systems, thereby introducing the concept of the Raman excitation profile which relates the laser frequencies over which resonant processes take place (Section 1.4.1 and 1.4.2). This leads to a discussion of Stokes and anti-Stokes spectra and the difference between the two (Section 1.4.3), followed by a discussion of the spectral width of particular phonon features in the Raman spectra (Section 1.4.4–1.4.6). Finally, we discuss

in Section 1.4.7, the characteristics of the Raman excitation profile, particularly the resonance window width.

1.4.1. *Raman spectra and the Raman excitation profile*

When we use one laser energy and observe the intensity of the scattered photons as a function of the shift of energy in cm^{-1} from the incident light (the Raman shift), this plot is called a Raman spectrum, from which we determine the phonon energy and its spectral width. The Raman spectrum is observed by passing the scattered light through a monochromator which divides the light entering the instrument into the scattered light on the lower energy side relative to the incident light (the so-called Stokes Raman spectra) and the scattered light on the higher energy side (the so-called anti-Stokes Raman spectra). At the zero energy shift, we generally see a strong Rayleigh signal which can be eliminated by using a so-called notch filter[5] or a (triple) monochromator.[6]

When we have an experimental laser system where the photon energy can be tuned (or changed), the Raman intensity for a low-dimensional sp^2 carbon system such as carbon nanotubes will show a sharp maximum at the resonance energy where the laser energy matches that of the excited states of the nanotubes. This resonant enhancement of the Raman intensities is called the resonance Raman effect. We denote the measurement of the Raman spectral intensity as a function of the laser energy as the Raman resonance window or the Raman excitation profile. The *resonance window* thus defined is normally expressed as the energy width at full-width at half-maximum (FWHM) intensity of the Raman intensity in the Raman excitation profile (which is a plot of the Raman intensity vs. E_{laser} in units of eV).

1.4.2. *Incident and scattered resonance conditions*

In the resonance excitation profile for an individual carbon nanotube, sharp maxima in the intensity are observed when the laser energy E_{laser} matches an optical transition energy E_{ii}, For a Raman-active phonon with an energy E_q, we expect two resonance conditions: $E_{\text{laser}} = E_{\text{ii}}$ and $E_{\text{laser}} = E_{\text{ii}} + E_q$ (for Stokes), which we call the incident and scattered resonance conditions, respectively. In the incident resonance condition, the initial photon absorption becomes a "real" absorption process, while in the scattered resonance condition, the final photon emission becomes a "real" emission process. For all Raman-active phonons, the resonance energy for the incident resonance is commonly E_{ii}, while the resonance energies for the scattered phonons depend on E_q. When the resonance window width in the Raman excitation profile is larger than E_q, we can see only one resonance peak. In the case of carbon nano-materials, a typical resonance window width is 50 meV and thus we can see two distinct peaks for optical phonons (0.2 eV), but not for RBM phonons (10–20 meV) in the case of SWNTs. It is important to note that the scattered resonance condition for the anti-Stokes Raman process is given by $E_{\text{laser}} = E_{\text{ii}} - E_q$.

1.4.3. *Stokes and anti-Stokes Raman processes*

The Stokes (S) and anti-Stokes (aS) processes for phonon scattering exhibit different Raman intensity behaviors from each other because the phonon number in the Stokes process is increased from n to $n + 1$ and this phonon creation process can always be carried out. However in the anti-Stokes process, a phonon is annihilated so that for the process to progress, phonons must be present to be annihilated and this may not be possible if the phonon energy is large compared to $k_{\text{B}}T$ where k_{B} is the Boltzmann constant. The average number of available phonons n at a

temperature T with energy E_q is given by the Bose–Einstein distribution function

$$n = \frac{1}{e^{E_q/k_B T} - 1}. \tag{2}$$

Of particular significance, room temperature (300 K) corresponds to 25.85 meV = 208.5 cm^{-1}. For carbon nanotubes the energies of the RBM phonons are comparable in energy to room temperature while the G-band and the D-band phonons are of much higher energies than the room temperature energy. Of particular significance is the relative magnitude of E_q relative to $k_B T$. Most Raman spectra are conveniently taken at room temperature (300 K),

As stated above, the probability for the S and aS processes differs because in the Stokes process the system goes from n phonons to $n + 1$, while in the anti-Stokes process (aS) the system goes from $n + 1$ to n. Using time reversal symmetry, the matrix elements for the transition $n \to n + 1$ (S) and $n + 1 \to n$ (aS) are the same, and the intensity ratio between the S and aS signals I_S/I_{aS} from one given phonon can be obtained by

$$\frac{I_S}{I_{aS}} \propto \frac{n+1}{n} = e^{E_q/k_B T}. \tag{3}$$

When we use Equation (3) for evaluating E_q or T, we must be careful not to be close to the resonance conditions for either the S or aS process. If E_{laser} corresponds to the resonance condition for $E_{laser} = E_{ii}$ for the incident photon, then all phonons will be in resonance in the Raman scattering process. But for $E_{laser} = E_{ii} \pm E_q = E_S$ only the scattered light is in resonance and although each phonon will be in resonance in the Raman spectrum of the nanotube, each phonon will be in resonance at a different E_S value.

1.4.4. *The Raman spectra and spectral width: Lorentzian lineshape*

A Raman spectrum is a plot of the scattered intensity I_S as a function of $E_{laser} - E_S$ (Raman shift, see Figure 7), and the energy conservation relation given by Equation (1) is a very important aspect of Raman spectroscopy. The Raman spectra will show peaks at a phonon energy $\pm E_q$, and in Figure 7 the energy of the Stokes process is shown at positive energy, while the anti-Stokes process is shown at negative energy in Figure 7. Thus, in the spectrometer (grating) which divides the scattered light into different directions, the anti-Stokes signal appears in the opposite position relative to the Stokes signal when measured from the central Rayleigh signal.

The Raman lineshape contains a wealth of information about the electrons and phonons for the various sp^2 nanocarbon systems. The Raman spectrum for semiconducting tubes exhibits a peak intensity $I(\omega)$ at a phonon energy of E_q displaced from E_{laser}. An expression for the frequency dependence of the phonon excitation can be obtained using a model based on a harmonic oscillator damped by some other interactions (similar to a mass-spring system inside a liquid). Therefore, the shape of the Raman peak will be the response of a damped harmonic oscillator with an eigenfrequency ω_q that is forced by an external field oscillating with a frequency ω. Considering the damping frequency to be given by Γ_q, the intensity $I(\omega)$ of a forced damped harmonic oscillator model of the phonon excitation is a Lorentzian curve

$$I(\omega) = \frac{I_0}{\pi \Gamma_q} \frac{1}{(\omega - \omega_q)^2 + \Gamma_q^2} \tag{4}$$

in the limit where the frequency $\omega_q \gg \Gamma_q$, where Γ_q is the damping term.[7]

The full width at half maximum intensity (*Raman spectral width*) is given by FWHM= $2\Gamma_q$. The center of the Lorentzian lineshape gives the natural phonon frequency ω_q, and Γ_q is related to

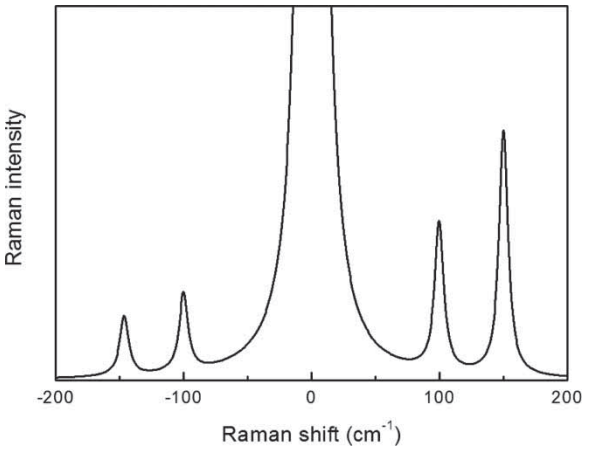

Figure 7. Schematics showing the Rayleigh line (at 0 cm^{-1}) and the Raman spectrum. The Rayleigh intensity is always much stronger and it has to be filtered out for any meaningful Raman experiment. The Stokes process (positive frequency peaks) are usually stronger than the anti-Stokes process (negative frequency peaks) due to phonon creation/annihilation statistics. Reprinted from Carbon, 48(5), M.M. Lucchese *et al.* pp. 1592–1597 [3]. Copyright © (2010) Elsevier.

the damping or the energy uncertainty or the phonon lifetime. The damping of the amplitude (as characterized by Γ_q) is observed as E_{laser} is tuned (and thus as the scattered light energy is varied). The damping of $I(\omega)$ thus provides information on the phonon lifetime, Δt. The uncertainty principle $\Delta E \Delta t \sim \hbar$ gives an uncertainty in the value of the phonon energy, as measured in the Raman spectrum, which corresponds to the spectral FWHM of $2\Gamma_q$. Therefore, Γ_q is the inverse of the lifetime for a phonon, and Raman spectra in this way provide information on phonon lifetimes.

There are two origins for the finite phonon lifetime: the anharmonic potential and the el–ph interaction, each of which are discussed below. This is followed by a further discussion of the lineshapes $I(\omega)$ observed for phonons.

(i) *Anharmonic potential*

Anharmonicity of the inter-atomic potential for the phonon occurs for large **r** far from the potential minimum. In this regime, the wave vector *q* of the phonon is no longer a good quantum number and phonon scattering occurs by emitting a phonon (third-order process) or by phonon–phonon scattering (fourth-order anharmonicity). Anharmonicity gives the main contribution to the thermal expansion process (third-order process) and to the thermal conductivity (fourth-order process).

(ii) *Electron–phonon interaction*

Another possible interaction is the el–ph interaction in which a phonon excites an electron in the valence band to the conduction band or scatters a photo-excited electron to other unoccupied states. The former el–ph process works for electrons in the valence band, while the latter el–ph process works for electrons in excited states. Thus, the origins of the finite lifetime of the phonon are different from each other for the case of electron and hole excitation, and is one mechanism for breaking the symmetry between electrons and holes in graphene.

1.4.5. *The Breit–Wigner–Fano (BWF) lineshape*

In specific cases, the Raman spectra can deviate from the simple Lorentzian lineshape in Equation (4). One obvious case is when the feature is actually composed of more than one phonon

contribution. Then the Raman peak will be a convolution of several Lorentzian peaks, depending on the frequency and weight of each phonon contribution.

One case of importance occurs when the lattice vibration couples to free electrons, as occurs in graphene or metallic nanotubes when an el–ph interaction takes place. In this case, additional line broadening and even distorted (asymmetric) lineshapes can result, and this effect is known as the Kohn anomaly (KA) [127]. In cases where phonons are coupled to the continuum excitation spectra of free electrons, the Raman peak may exhibit a so-called Breit–Wigner–Fano (BWF) lineshape, given by [128,129]

$$I_{\mathrm{BWF}}(\omega) = I_0 \frac{[1 + (\omega - \omega_{\mathrm{BWF}}/q_{\mathrm{BWF}}\Gamma_{\mathrm{BWF}})]^2}{1 + [(\omega - \omega_{\mathrm{BWF}}/\,\Gamma_{\mathrm{BWF}})]^2}, \tag{5}$$

where $1/q_{\mathrm{BWF}}$ is a measure of the interaction of a discrete level (the phonon) with a continuum of states (the electrons). Here ω_{BWF} is the BWF peak frequency at the maximum intensity I_0, and Γ_{BWF} is the frequency half width-half maximum for the intensity profile of the BWF peak. Such effects are observed in certain metallic sp^2 carbon materials and are discussed later, in connection with metallic carbon nanotubes.

1.4.6. *The effect of defects on spectral broadening*

In a perfect system, the one-phonon Raman intensity $I_0(\omega)$ associated with a vibrational mode of wavevector $\mathbf{q}_0$ and frequency $\omega(\mathbf{q}_0)$ is well described by a Lorentzian function

$$I_0(\omega) \propto \frac{1}{[\omega - \omega(\mathbf{q}_0)]^2 + [\Gamma_0/2]^2}, \tag{6}$$

as described above. A disordered distribution of point defects as would be produced by ion implantation, however, will scatter phonons and will also add a contribution to the FWHM by coupling phonons of wavevector $\mathbf{q}_0$ to those of wavevector $\mathbf{q}_0 + \delta\mathbf{q}$ [130]. In the limit of low levels of disorder, the coupling will be most effective for small δq, so the phonon wave packet in k-space can be described by a Gaussian function $\exp[-(\mathbf{q} - \mathbf{q}_0)^2 L_{\mathrm{pc}}^2/4]$ centered at $\mathbf{q}_0$ and having a width proportional to $1/L_{\mathrm{pc}} \approx \delta q$. Therefore, in real space L_{pc} is a measure of the phonon coherence length, which should also be a good measure of the average distance between point defects. Then, the Raman intensity for the disordered graphene $I(\omega)$ can be written as [130–134]

$$I(\omega) \propto \int_{BZ} d^2q \frac{W(\mathbf{q}) \exp\left[-(\mathbf{q} - \mathbf{q}_0)^2 L_{\mathrm{pc}}^2/4\right]}{[\omega - \omega(\mathbf{q})]^2 + [\Gamma_0/2]^2}, \tag{7}$$

where the integral is taken over the 2D BZ of graphene and $W(\mathbf{q})$ is a weighting function that describes the wavevector dependence of the el–ph coupling for the Raman process.

1.4.7. *The Raman resonance window*

Here, we consider the Raman excitation profile or the Raman resonance window, including the width of the resonance window γ_r. Both the lineshape and the width of the resonance window are considered when obtaining information from the excitation profile. In principle, the Raman intensity $I(E_{\mathrm{laser}})$ for a 1D or zero-dimensional carbon sp^2 system shows a dependence on the laser energy E_{laser} in the Raman excitation profile associated with resonances of E_{laser} with the

incident $E_{\rm ii}$ and scattered light $E_{\rm ii} \pm E_q$ according to

$$I(E_{\rm laser}) = \left| \frac{A}{(E_{\rm laser} - E_{\rm ii} - {\rm i}\gamma_r)(E_{\rm laser} - (E_{\rm ii} \pm E_q) - {\rm i}\gamma_r)} \right|^2, \tag{8}$$

where the resonant lineshape $I(E_{\rm laser})$ consists of two peaks at $E_{\rm laser} = E_{\rm ii}$ (*incident resonance condition*) and $E_{\rm laser} = E_{\rm ii} \pm E_q$ (*the scattered resonance condition*). Here γ_r is the FWHM width discussed below. Experimentally it is not always possible to resolve the observed $I(E_{\rm laser})$ lineshape into two peaks.

The FWHM width of each peak in the Raman excitation profile is the resonance window width γ_r, and is related to the lifetime of an electron in its excited states. If the lifetime of the photo-excited electron is finite, then the resonance condition in the Raman excitation profile may show departures from Equation (8) which assumes $\gamma_r \ll E_q$. The finite lifetime of the photo-excited electron is subject to the uncertainty relation $\Delta E \Delta t \sim \hbar$.

The photo-excited carrier can be relaxed from the excited states by several processes, each occurring according to different time scales:

- The Coulomb interaction between electrons (10–100 fs).
- The electron–phonon interaction for all possible phonons (with lifetimes < 1 ps).
- The electron–photon interaction (with lifetimes < 1 ns).

When we consider the Coulomb interaction for a given electron, the other electrons should excite the first electron to an unoccupied state. Thus, the Coulomb interaction depends on the metallicity of the material. In the case of carbon nanotubes, the interaction between two excitons that is relevant to this term is known as the Auger process. On the other hand, a photo-excited electron has a definite lifetime for emitting any energy–momentum conserved phonon. Thus, the el–ph interaction of the electron from a state k (a photo-excited state) to the energy–momentum conserved $k + q$ (phonon emitting electron state) is important. Note that γ_r (the resonance window width, Eq. (8)) is physically different from Γ_q (the Raman spectral width, Eq. (4)).

1.5. *Raman measurements of low-dimensional materials*

The resonance Raman effect is especially important in low-dimensional nano-systems since the density of states becomes singular (because of the presence of van Hove singularities in 1D systems, see Figure 8) and the spectral energies become discrete. The latter effect is important for decreasing the resonance window width since the number of energy–momentum conserved intermediate states becomes small and thus the corresponding lifetime of the photo-excited carrier becomes long. These are the reasons why we can observe Raman spectra even from a single molecule or, for the case of carbon sp^2 nanostructures, we can even see Raman spectra from an individual carbon nanotube.

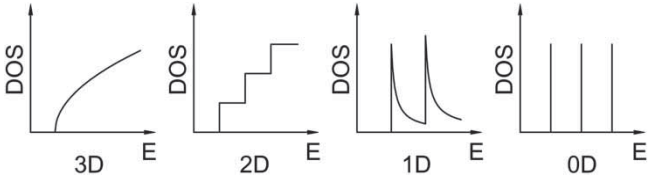

Figure 8. Typical electronic density of states for 3D, 2D, 1D and 0D systems.

1.5.1. *Cutting lines and van Hove singularities of the density of states*

When the 2D sheets of graphene are rolled up to form 1D nanotubes, different subbands in the 1D reciprocal space of the nanotube can be extended into the 2D reciprocal space of a single sheet of the parent bulk layered material as a set of parallel equi-distant cutting lines [32,135,136]. This procedure is shown in Figure 9(a) for states near the K point.

Figure 9(b) shows the electronic density of states (DOS) related to the nanotube electronic band structure plotted schematically in Figure 9(a). Each of N cutting lines in Figure 9(a) (except for the one that crosses the degenerate K point) gives rise to a local maximum in the DOS $g(E)$ in Figure 9(b), known as a (1D) van Hove singularity (vHS), given by

$$g(E) = \frac{2}{N} \sum_{\mu=1}^{N} \int \left[\frac{\partial E_\mu(k)}{\partial k} \right]^{-1} \delta[E_\mu(k) - E] \, \mathrm{d}k. \tag{9}$$

The four vHSs in Figure 9(b) are labeled by $E_{\mathrm{i}}^{(\mathrm{v})}$ and $E_{\mathrm{i}}^{(\mathrm{c})}$ for the electronic subbands in the valence and conduction bands, correspondingly. The presence of vHSs in the DOS of 1D structures makes these structures behave differently from their related 3D and 2D counterpart materials, as can be seen in Figure 8. A finite density of states between the first singularities in the valence band and conduction band for metallic nanotubes is shown in Figure 9(b).

1.5.2. *Dimensionality and the resonance Raman effect*

The electronic DOS profiles for systems of different dimensionality (3D, 2D, 1D, and 0D) are very different from one another, as shown in Figure 8. The typical DOS dependence on energy near an

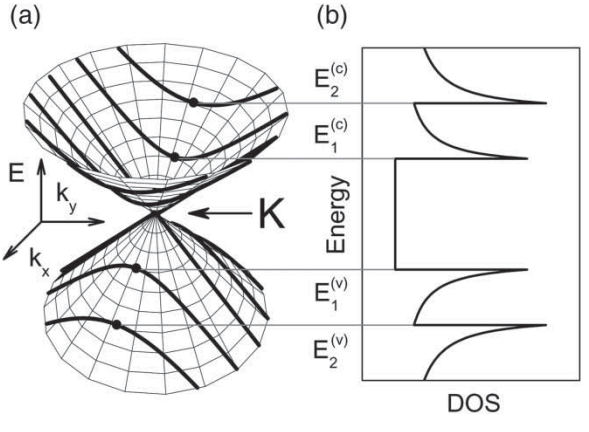

Figure 9. (a) The energy–momentum contours for the valence and conduction bands for a 2D system, with each band obeying a linear dependence for $E(k)$ and forming a degenerate point K where the valence and conduction bands touch to define a zero gap semiconductor. The cutting lines of these contours denote the dispersion relations for the 1D system derived from the 2D system. Each cutting line gives rise to a different energy subband. The energy extremum E_{i} for each cutting line at the wave vector k_{i} occurs at a van Hove singularity. The energies $E_{\mathrm{i}}^{(\mathrm{v})}$ and $E_{\mathrm{i}}^{(\mathrm{c})}$ for the valence and conduction bands and the corresponding wave vectors $k_{\mathrm{i}}^{(\mathrm{v})}$ and $k_{\mathrm{i}}^{(\mathrm{c})}$ at the van Hove singularities are indicated on the figure by the solid dots. (b) The 1D density of states (DOS) for the conduction and valence bands in (b) corresponding to the $E(k)$ dispersion relations for the 1D subbands shown in (a) as thick curves. The DOS shown in (b) is for a metallic 1D system, because one of the cutting lines in (a) crosses the degenerate Dirac point (the K point in the graphite Brillouin Zone (BZ)). For a semiconducting 1D system, no cutting line crosses the degenerate point, thus resulting in a band gap opening up in the DOS between the van Hove singularities $E_1^{(v)}$ and $E_1^{(c)}$ [135].

energy band extremum, $g(E)$ is given by $g \propto (E - E_0)^{[(D/2)-1]}$, where D is an integer, denoting the spatial dimension and D assumes the values 1, 2, and 3, respectively, for 1D, 2D, and 3D systems [137]. The parameter E_0 appearing in the density of states $g(E)$ denotes the energy band minimum (or maximum) for the conduction (valence) energy bands. For a 1D system, E_0 would correspond to the energy of a vHS in the DOS occurring at each subband edge, where the magnitude of the DOS becomes very large. One can see from Figure 8 that 1D systems exhibit DOS profiles which have some similarity to the case of 0D systems, with both 0D and 1D systems having very sharp maxima at certain energies, in contrast to the DOS profiles for 2D and 3D systems, which show a more monotonic increase with energy (see Figure 8). However, the 1D DOS is different from the 0D DOS (δ function at each discrete energy level) in that the 1D DOS has a sharp threshold and a decaying tail for each cutting line, so that the 1D DOS does not go to zero between the sharp maxima, as the 0D DOS does (see Figure 8). This is even true for semiconducting nanotubes which have a finite band gap and no occupied states between the first cutting lines in the valence and conduction bands. The extremely high values of the DOS at the vHSs allow us to observe physical phenomena for individual 1D nanostructures in various experiments, as discussed in Section 1.1.6.

1.5.3. *Coherence time and length in Raman processes*

It is not trivial to define whether a real system is large enough to be considered as being effectively infinite and therefore to exhibit a quasi-continuous phonon (or electron) energy dispersion relation. Whether or not an explicit dispersion relation can be defined indeed depends on the process that is under evaluation and the characteristics of this process. In the Raman process, we ask how long does it take for an electron excited by the incident photon to decay? Considering this Raman scattering time, what is the distance probed by an electron wave function? These issues are discussed in condensed matter physics textbooks [119] under the concept of *coherence*. The coherence time is the time the electron takes to experience an event such as a scattering process that changes its state. Thus, the coherence length is the distance over which the electron maintains its quantum state identity and its phase coherence. The coherence length is defined by the electron speed and the coherence time, both of which can be measured experimentally. The Raman process is an extremely fast process, and is in the range of femto-seconds (10^{-15} s). Considering the speed of electrons in graphite and graphene (10^6 m/s), this electron speed gives a coherence length of the order of nm. Interestingly, this number is much smaller than the wavelength of visible light. On the other hand, this is a particle picture for the scattering process and consideration of both the particle and wave aspects of electrons and phonons (as well as excitonic effects) are important for carbon sp^2 nanostructures. The study of such concepts is actually very interesting and important when dealing with local processes induced by defects, as discussed later (Section 4.3) in this article.

2. Experimental progress of Raman spectroscopy and related optics

As shown in Figure 10, the use of photo-physical techniques has contributed a great deal to our understanding of carbon nanostructures because of the large amount of information photo-physical techniques have provided and the relative simplicity of many of these experimental techniques. The resonance Raman effect and the strong el–ph coupling of carbon nanotubes and graphene, together with the simplicity of sample preparation required for Raman experiments when compared with many other techniques, elevate Raman spectroscopy to a special position. Raman spectrometers are broadly available and generally easy to use. For this reason, Raman spectroscopy is the most common sample characterization tool used by groups working with carbon nanotubes and graphene.

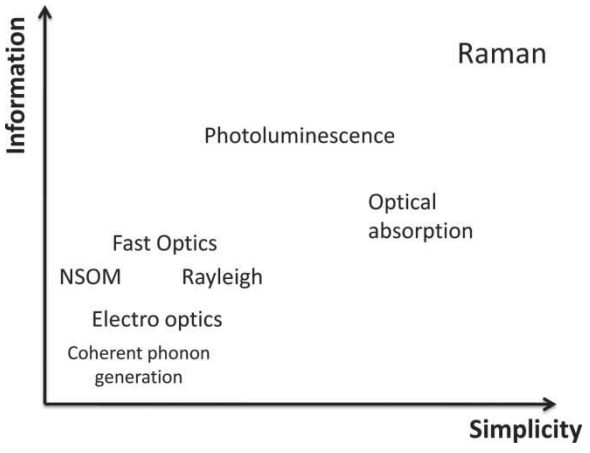

Figure 10. Qualitative comparative evaluation of the amount of information vs. the simplicity of performing an optical experiment in SWNTs based on the experience of the authors. The position of each technique in the plot is defined both by phyiscal limitations (e.g. photoluminescence is not available from metallic SWNTs) and by aspects of practical implementation.

In Section 2, we review a number of optical and spectroscopic techniques that are used for characterizing materials and especially focusing on sp^2 carbon materials, carbon nanotubes and graphene. We start this section with a brief introduction to the special properties of electrons and phonons in graphene.

2.1. *Electrons and phonons in graphene*

In order to analyze optical phenomena and Raman spectra of sp^2 carbons, we focus on the electronic and vibrational structure of graphene, the mother material of sp^2 carbons. In this section, we review the geometrical structure, the electronic structure and the phonon structure of graphene.

2.1.1. *The hexagonal crystal structure of graphene*

Mono-layer graphene (1-LG) is a single atomic layer of graphite in which carbon atoms crystallize into a hexagonal lattice (see Figure 2). The unit cell of the hexagonal lattice is a rhombus which consists of two distinct carbon atoms A and B (see Figure 2(a)). The first BZ of graphene shown in Figure 2(e) also has a hexagonal periodicity in k space.

2.1.2. *The electronic structure and optical transitions*

The carbon valence electrons of graphene have $2p_z$ orbitals. This orbital is elongated in the direction perpendicular to the C–C bond and therefore is called a π orbital.[8] A simple tight-binding calculation for the two π orbitals for the A and B atoms in the unit cell gives two π energy bands. The electron-occupied band is called the π band and the electron-unoccupied band is called the π^* band. Of particular interest is the fact that the two π energy bands touch each other at the K and K' points which are the two non-equivalent hexagonal corners of the BZ where the Fermi energy for undoped graphene is located. What is special about the π bands in graphene is that the energy dispersion of both π bands near the K and K' points have the same linear $E(k)$ relation. Thus, the corresponding electron and hole effective masses at the K and K' points become zero,

and increase as we move away from the K and K' points. The anomalous and symmetric behavior of the electrons and holes in graphene mainly originates from this unusual linear $E(k)$ energy dispersion relation of graphene near the Fermi energy, E_F.

Electronic transitions occur from the electron-occupied π band to the electron-unoccupied π^* energy band. Selection rules forbid intra-atomic transitions from 2p to 2p states. However, inter-atomic transitions from 2p to 2p states are allowed both for the nearest-neighbor pairs of carbon atoms and for further neighbors as well. Since the energy dispersion is linear near the K and K' points, the electronic dispersion in graphene forms Dirac cones. Optical transitions for a given laser excitation energy E_{laser} occur on the equi-energy lines around the K and K' points. Because of the three-fold symmetry of $E(k)$ around the K or K' points, the equi-energy lines are distorted into a triangle with increasing energy [32,138]. This trigonal warping effect of the energy dispersion and of the Fermi surface dominate the electronic properties.

2.1.3. *Phonons and the el–ph interaction in graphene*

The two carbon atoms in the graphene unit cell result in six phonon modes and six energy dispersions in the unit cell [1]. Three of the six phonon modes are acoustic (A) phonon modes whose phonon energy is zero at the zone center of the BZ (the Γ point). The other three phonon energy bands correspond to optical (O) phonon modes in which the vibration directions of the A and B atoms are anti-symmetric with respect to each other. The three A (or O) phonon modes consist of one longitudinal (LA or LO) mode and two tangential (TA or TO) phonon modes. The two tangential phonon modes (TA or TO) consist of one in-plane (iTA and iTO) and one out-of-plane (oTA and oTO) phonon mode. Since the L phonon modes of graphene are always in-plane phonon modes, the i label for the LA and LO phonon modes is generally suppressed. Hexagonal symmetry requires a degeneracy for the LO and iTO phonon modes at the Γ point and for the LA and LO modes at the K points.

The electron motion of the A and B carbon atoms is perturbed by the atomic vibrations which cause an electron to scatter from a k state to a $k+q$ state by emitting a $-q$ phonon. In Raman spectroscopy, we generally consider the el–ph interaction for a photo-excited electron within a π^* energy band. There is thus a restriction imposed on the scattering event that the final state must be unoccupied. Energy and momentum conservation applies to the scattering of electrons by emitting a phonon, resulting in a maximum energy for $E(k) - E(k+q)$ which corresponds to the maximum phonon energy (0.2 eV for graphene). The scattering of electrons only occurs within circles of equi-energy which specify the allowed optical transitions. Since we have two Dirac cones which are near the K and K' points, this restriction does not mean that the momentum transfer q is restricted to lie within the equi-energy circle. Electron scattering from the K to K' (or from the K' to K) regions is possible, for energy differences between the incident and scattered photons up to 0.2 eV, and we call these processes inter-valley scattering processes [139]. On the other hand, scattering within each of the K or the K' regions can also occur and this type of scattering is called an intra-valley scattering event. Another important concept for electron and phonon scattering is the distinction between forward and backward scattering. The velocity of the electron can change its sign upon scattering, since its group velocity is given by $\partial E(k)/\partial k$. If the scattered states are on the same (another) side of a Dirac cone, then the scattering event is classified as forward (backward) scattering. Considering the six phonon modes, the two types of valley scattering processes, and both forward and backward scattering processes, there are 24 different possible types of scattering processes that are relevant to the el–ph interaction and all of these 24 scattering processes are discussed below.

2.2. *Electrons and phonons in 1D carbon nanostructures*

2.2.1. *1D carbon structures*

Carbon nanotubes [32] and graphene nanoribbons [140] are 1D sp^2 carbon nanostructures based on graphene and their physical properties can be discussed by zone-folding the 2D dispersion relations of graphene onto the 1D BZs of carbon nanotubes and graphene nanoribbons both of which have discrete wave vectors which are specified in the quantum confined direction. Both carbon nanotubes and graphene nanoribbons have a 1D unit cell for which translational symmetry exists, respectively, along the direction of the nanotube axis and the ribbon axis. The quantum confinement of electrons and phonons in the circumferential direction of nanotubes or along the ribbon width direction of nanoribbons applies to their discrete wavelengths and discrete wavevectors, which are expressed by the cutting lines discussed in Section 1.5. The symmetries of the 1D unit cells are given by point group theory which specifies the possible Raman-active modes and the possible dipole-allowed optical transitions [141,142].

2.2.2. *π bands and phonons in carbon nanotubes and nanoribbons*

The electronic dispersion relations for the π (π^*) bands of carbon nanotubes and graphene ribbons consists of $2N$ energy subbands, where $2N$ denotes the number of carbon atoms in the 1D unit cell. Each energy subband is obtained from the 2D energy bands of graphene by combining the pertinent allowed 1D wave vectors on a cutting line in the 2D BZ of graphene. For zigzag graphene ribbons, special electronic states, called edge states appear for which the amplitude of the wavefunction is localized at one zigzag edge and on one sublattice (A or B) of graphene [140], and these zigzag edge states have a very high density of electronic states at the Fermi level [143]. The density of states for zigzag nanotubes including the spin–orbit interaction was calculated by Son and Louie [143,144].

The phonon dispersion of carbon nanotubes and graphene nanoribbons similarly contain $2N$ energy subbands. Most phonon subbands are also obtained by combining the zone-folding of the 2D phonon dispersion relations and using appropriate cutting lines. However, in the case of carbon nanotubes, special phonon modes which do not appear in graphene must be introduced to describe carbon nanotubes. These additional phonon modes are the RBM and the twist modes (TM), in which the carbon atoms are vibrating along the radial direction and along specific directions with respect to the nanotube axis [32].

2.2.3. *Optical transitions*

Special to 1D systems is the quantum confinement of discrete k vectors associated with the van Hove singularities in the 1D DOS for the top and bottom of each energy subband of the π bands (see Figure 9). When the light is polarized along the nanotube axis or along the graphene ribbon axis, optical transitions occur between π and π^* energy bands at the same cutting line for the initial and final state and a strong absorption occurs from the top of the π bands to the bottom of the π^* band at the wavevector k_{ii}. For 1D systems, the k_{ii} vector is special because the joint density of states (JDOS) for the ith π band and the ith π^* band become singular at the energy separation of E_{ii}. For light perpendicular to the nanotube axis, optical transitions occur between nearest-neighbor cutting lines with energies $E_{\mathrm{i},i+1}$ because the polarized light in this case has an additional quantum unit of angular momentum. Thus, different selection rules apply to light polarized parallel (E_{ii}) or perpendicular ($E_{\mathrm{i},i+1}, E_{\mathrm{i},i-1}$) to the nanotube or graphene ribbon axes.

2.2.4. *Type I and II semiconductor nanotubes*

In discussing optical transitions, it is important to classify (n, m) semiconducting nanotubes into two categories depending on whether $\mathrm{mod}(2n + m, 3) = 1$ or 2, which we call Types I or II

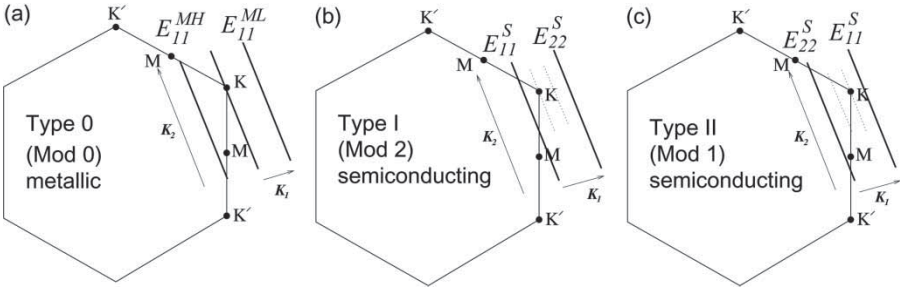

Figure 11. Cutting lines near the K point in the 2D BZ of graphene for (a) Type 0 (or Mod 0) metallic SWNTs, (b) Type I (Mod 2) and (c) Type II (Mod 1) semiconducting SWNTs.

semiconducting nanotubes (S-SWNTs), respectively.[9] In Figure 11, we show the geometry of the cutting lines near the K point in the 2D BZ of graphene. In the case of type I (II) semiconducting nanotubes, the K point lies at the one-third (two-thirds) position between two cutting lines, since the distance of the K point from the cutting line at the Γ point is given by $(2n + m)/3$ times K_1, where K_1 is a reciprocal lattice vector in the direction of the chiral vector [32]. In Figure 11(a), we see that $\mathrm{mod}(2n + m, 3) = 0$ corresponding to metallic nanotubes. Each cutting line results in an optical transition for its E_{ii} value. Further discussion of this classification is given in [107,135, 136,141,145,146]. Because of the anisotropy of the effective mass tensor around the K point, the optical properties of S-SWNTs depend on their Type I or II classification (see Figure 11(b) and (c)). We call this classification the semiconductor type-dependence.[1]

2.2.5. *1D exciton, exciton–photon and exciton–phonon interactions*

For a pure 1D electron and hole pair, such as that occurs for a carbon nanotube or a graphene ribbon, the exciton binding energy becomes singular (∞ energy) for the lowest energy state. For a nanotube or a nano-ribbon, however, the binding energy of these nanostructures is also finite, since the nanotube circumference or nanoribbon width is finite. Though finite, the binding energy is still very large for a 1 nm diameter nanotube or a nanoribbon of 1 nm width, compared with the room temperature thermal energy of 25 meV. Thus, understanding excitonic electron and hole binding is essential for understanding the optical properties of nanotubes at room temperature.

Since the exciton is localized in real space, the exciton wavefunction is given by a linear combination of many wave vector states near the k_{ii} points, whose mixing coefficients are given by the Coulomb interaction between the photo-excited electron and the valence electrons (electron self-energy) or between a photo-excited electron and hole (exciton-binding energy). These exciton wavefunctions for graphene ribbons or nanotubes are calculated by the Bethe–Salpeter equation [120,147,148]. Because of the highly localized wavefunction of an exciton, the intensity of the excitonic optical transition (absorption and emission) intensity is enhanced significantly (10,000 times) relative to ordinary optical excitations between conventional band states. On the other hand, since the el–ph interaction strongly depends on the wavevectors k near the Fermi energy, the exciton–photon interaction energy (which is given by the integration of the el–ph interaction over k weighted by the exciton wavefunctions) shows a strong (n, m) dependence. In fact, the value of the exciton–phonon interaction is of the same order of magnitude as the el–ph interaction in these 1D systems. The observation of excitons in carbon nanotubes was first reported by the Heinz group at Columbia [44,121] and by the Reich–Thomsen group in Berlin [122].

2.3. *The optical measurement techniques*

In this section, we mention the various measurement techniques which have been used to study the photophysics of carbon nanotubes, graphene and graphene nanoribbons. In general, the studies on carbon nanotubes are more developed, while graphene and graphene nanoribbons are still in an early stage. Some techniques are found to be more sensitive for certain systems and others may be more sensitive for the specific applications that a particular system might be used for. It is also important to know which photophysical techniques have been or could be used for spectroscopic studies and for making related measurements on graphene, graphene nanoribbons, carbon nanotubes and related sp^2 nano-carbon systems. These various techniques are briefly reviewed in this section.

2.3.1. *Light absorption*

Light absorption is one of the most fundamental photophysical measurement techniques. A typical absorption spectrum is shown in Figure 12(a). This spectrum compares the optical absorption spectra in 1D SWNTs to that in colloidal 3D graphite. Above 2.0 eV, the spectrum of the two carbon forms is similar. At lower energies, however, the SWNT sample shows three broad peaks, A, B and C in Figure 12(a), associated with the two lowest allowed transitions in semiconducting SWNTs (A, E_{11}^S and B, E_{22}^S shown in Figure 12(b)) and the first peak in the joint density of states (JDOS) of the metallic nanotubes (C, E_{11}^M shown in Figure 12(b)). Measurements on isolated SWNTs show sharper transitions than for SWNT bundles, and each sharp transition is related to specific van Hove singularities, relevant to each SWNT. These transitions become merged and broadened in samples of nanotube bundles.

Graphene, being a 2D system, has no such van Hove singularities[10] and the optical absorption of 2D graphene looks more similar to that of 3D graphite [42,149]. However, for a given optical frequency, the optical absorption of graphene depends on the number of graphene layers. The amount of light transmitted through an N-layer graphene sample only depends on N and on fundamental constants. Experiments have confirmed the theoretically expected universal value $\pi e^2/hc$ for the optical conductivity of graphene [74] (or a 2.3% optical absorption per graphene layer). Such experiments have also revealed departures of the quasi-particle dynamics from the

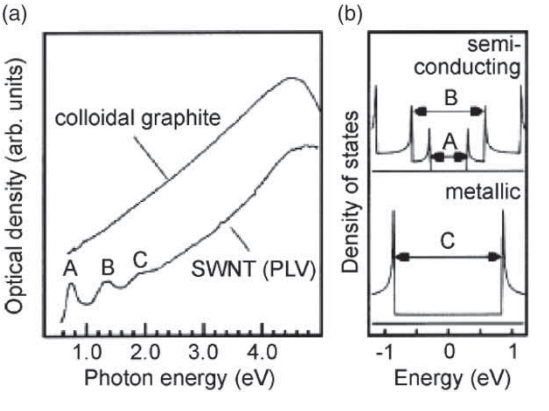

Figure 12. (a) The optical absorption spectra from SWNTs and from colloidal graphite shown comparatively. (b) Illustration of interband processes giving rise to the optical absorption peaks in semiconducting and metallic SWNTs [42].

simple predictions for Dirac Fermions in idealized graphene as we move sufficiently far from the Dirac point in k space.

2.3.2. *Resonance Rayleigh scattering*

Rayleigh scattering refers to the elastic scattering of light and the intensity of the Rayleigh scattered light intensity in graphene depends on the number of graphene layers and this technique can be used for determining the number of layers in a given few layer graphene sample. The Rayleigh scattering intensity is stronger when the laser is in resonance with an optical transition energy in which case the process is called resonance Rayleigh scattering. An important use of resonance Raleigh scattering is to directly measure the E_{ii} values of SWNTs when using the laser light source whose frequency can be tuned. Figure 13(a) shows a schematic representation of the dark-field configuration which is used for this type of Rayleigh scattering spectroscopy. This geometry is used to efficiently reject the incident laser light so that the nearby Rayleigh signal can be clearly seen. One main challenge of Rayleigh scattering experiments comes from sample preparation. In this application, isolated SWNTs are prepared by chemical vapor deposition (CVD) and a substrate with a slit etched in it is used, allowing exploitation of the dark-field configuration shown in Figure 13(b). In the experiment of Figure 13(a), typical slit widths are tens of micrometers and slit lengths are up to 1 mm [44,150].

Since the pioneering work of the Heinz group [150], Rayleigh scattering is becoming increasingly popular as a method for the rapid identification of the (n, m) indices of individual SWNTs. Figure 14 shows the Rayleigh spectrum of different (n, m) SWNTs for the type of sample shown in Figure 13(b). The (n, m) of individual SWNTs are identified by comparing the observed resonance peak frequencies with the expected theoretical values, anchored on some geometrical constraints that are discussed in more detail from a theoretical standpoint in Section 3. For example, in Figure 14(a) the (16,11) type I S-SWNT has a similar electronic structure to the (15,10) type I SWNT, and the resonance Rayleigh spectra of both are displayed together in Figure 14(a). The diameter of the (16,11) nanotube is 1.83 nm, which is 0.12 nm greater than the 1.71 nm diameter

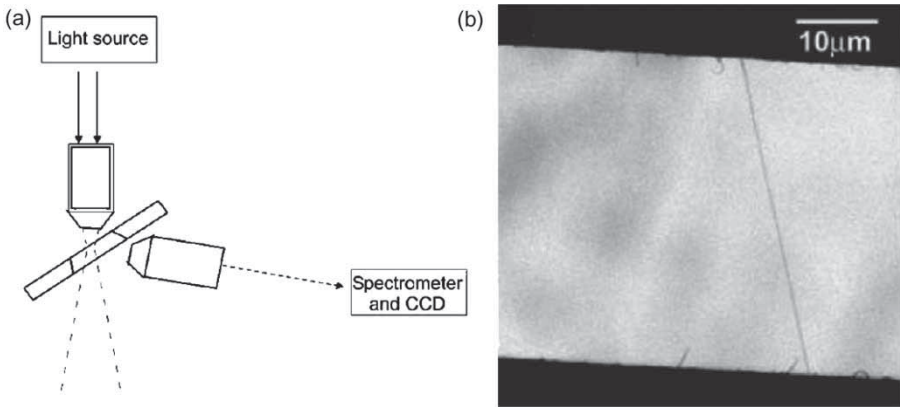

Figure 13. (a) Schematic diagram for a Rayleigh scattering measurement. Microscope objectives focus the incident light on a suspended nanotube and collect the radiation of the scattered light. Using a super-continuum source, different wavelengths can be detected simultaneously using a spectrometer and a multichannel (CCD) camera. (b) Electron micrograph of an individual suspended SWNT in a geometry used for Rayleigh scattering spectroscopy. Adapted from Carbon Nanotubes: Advanced Topics in the Synthesis, Structure, Properties and Applications, T.F. Heinz [44]. Copyright (2008) from Springer.

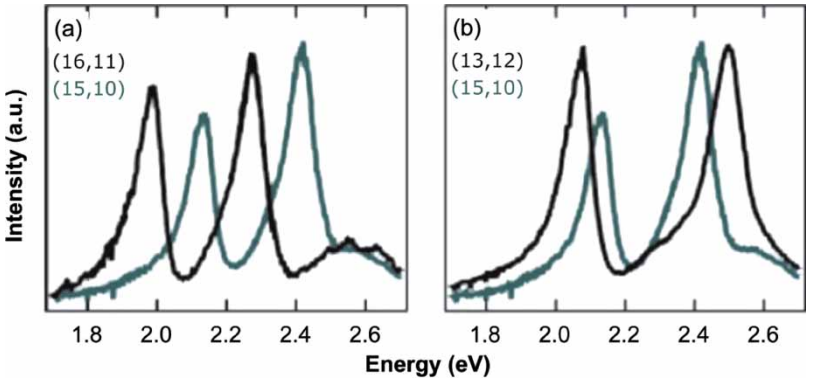

Figure 14. The Rayleigh scattering spectra of two different (n, m) semiconducting SWNTs shown comparatively for type I(a), type II(b) semiconducting SWNTs. The peaks in both cases correspond to the E_S^{33} and E_S^{44} interband transitions. The comparison in (a) corresponds to two nanotubes of the same $(2n + m)$mod3 type, but having different diameters; the comparison in (b) corresponds to two nanotubes of different type, but with similar SWNT diameters. Adapted from M.Y. Sfeir *et al.* Science, 312, pp. 554–556, 2006, [150]. Adapted with permission from AAAS.

of the (15,10) SWNT. As a result, a downshift of about 150 meV in the E_{33}^S and E_{44}^S transitions of the larger diameter nanotube is observed. The ratio of the E_{44}^S to E_{33}^S transition energies is similar for these two nanotubes which are both of type I S-SWNT. However, a comparison of the (13,12) type II S-SWNT with the (15,10) type I S-SWNT (Figure 14(b)) shows a different behavior for the two different types of S-SWNTs. In this case, the average energies of the two transitions of the (15,10) and (13,12) nanotubes are very similar due to their nearly identical diameters (1.71 nm and 1.70 nm, respectively). However, the difference in behavior is manifested in the dissimilar intensity ratios for their E_{44}^S to E_{33}^S transitions. Rayleigh scattering measurements have been especially useful for advancing the theory related to optical transition energies in SWNTs and how environmental effects influence these values [44]. Rayleigh scattering experiments have also been carried out in graphene by Casiraghi [151].

2.3.3. *Photoluminescence excitation spectra*

The photoluminescence technique has become an especially popular method for characterizing semiconducting SWNTs [152,153]. The photoluminescence excitation (PLE) spectra conveniently characterize S-SWNTs by measuring their emission spectra and the technique is limited to semiconducting nanotubes. The PLE spectrum thus plots the light emission as a function of the laser excitation energy of the light and most experiments focus on measuring E_{11}^S rather than higher E_{ii}^S with PLE [152,153]. Here, we show a PLE spectrum for a semiconducting-(6,5)-enriched SWNT sample, illustrated in Figure 15 [154], in order to show several light scattering peaks (highlighted by circles in Figure 15(b)), which also include Raman scattering events in addition to PLE. The vertical gray band in Figure 15(a) denotes photoluminescence emission at the band gap $E_{PL} = E_{11} = 1.26$ eV. The horizontal gray bands denote nearly continuous-luminescence emission bands associated with thermally excited processes involving different phonon branches for the (6,5) SWNT. The cutoff energy at 1.06 eV is marked in Figure 15(b) by a vertical dotted line which corresponds to the maximum phonon energy $(1.26 - 1.06 = 0.20$ eV) in the first-order phonon spectra. Slanted dotted lines, which correspond to $E_{ex} - E_{em} =$ constant, denote emission from resonance Raman spectra (RRS) for G-band, M-band and G′-band phonons. Note that the strong

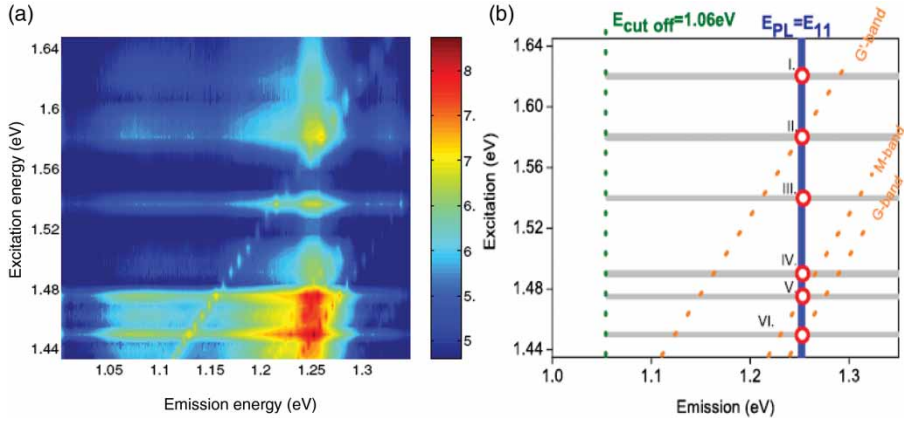

Figure 15. (a) A 2D excitation vs. emission contour map for a dried (6, 5)-enriched DNA-CNT sample on a sapphire substrate. The spectral intensity is plotted using the log scale shown on the right. (b) A schematic view of the various observed light emissions plotted as the laser excitation energy vs. photon emission energy. Reproduced figure with permission from S.G. Chou *et al.* Physical Review Letters 94, p. 127402, 2005 [154]. Copyright © (2005) by the American Physical Society.

emission spots, appearing in Figure 15(a) at E_{11} and denoted by circles, correspond to energies where these bands cross the E_{11} transition energy. These intersection points are associated with a mixture of PL and RRS processes involving one-phonon (VI) and two-phonon (I–V) processes, following the labels in Figure 15(b). The various features in Figure 15 differ in linewidth. The Raman peaks are much sharper (tens of cm^{-1}) than the PL peaks which have linewidths of hundreds of cm^{-1}. The various peaks also differ by the fact that, when changing the excitation laser energy, the PL emission is fixed at E_{11}, while the Raman peaks change in frequency, keeping fixed the energy shift from E_{laser}. With light emission occurring at the same energy, the PL and RRS processes are sometimes confused in the literature, and the major reason is that RRS in solids often has a much greater (typically 10^3 times larger) intensity than the non-resonance Raman spectra [155]. To differentiate between the RRS and PL processes, one can just look at what happens to the spectral output when changing E_{laser}.

The difference in linewidth between RRS and PL arises because in Raman scattering the intermediate states that are excited between the initial state (incident photon plus the energy of the system before light absorption) and the final state (emitted photon plus the energy of the system after light emission) are "virtual" states.[11] These virtual states do not have to correspond to real states (and do not have to be eigenstates of the physical "system") – any optical excitation frequency will, in principle, suffice in RRS. In photoluminescence, on the other hand, the optically excited state must be a real state of the system, and PL involves a real absorption of light at one frequency, followed by a real emission of light at a different frequency.[12] Photoluminescence is a technique commonly used to study graphene samples engineered for an energy gap opening but studies of energy gap opening are still at an early stage.

2.3.4. *Electro-luminescence*

Light emission by excited carriers can also be obtained by means other than photo-excitation, such as electro-luminescence (EL). In EL the electrically induced excitation is followed by ambipolar e–h recombination which comes from electrons and holes that are injected independently by using doped semiconductor electrodes and impact excitation occurs by hot carriers. These effects have

largely been studied in SWNTs [47,156,157], where both radiative decay of photo-excited and electron-excited emission occur, as well as the non-radiative decay to create free carriers which can then be studied by their photoconductivity spectra. EL processes could lead to the technological use of carbon nanotubes as nanometer scale light sources and as photo-current or photo-voltage detectors. EL has also been observed in graphene [157].

2.3.5. *Infrared absorption spectroscopy*

IR absorption spectroscopy has especially been useful for characterizing nanotubes [158–160]. In the case of graphene the IR absorption per layer of graphene is 2.3% and is given by the simple formula [74]

$$\pi\alpha = \pi\left(\frac{e^2}{\hbar c}\right) = 2.293\% \tag{10}$$

and for this reason can be used to determine the number of graphene layers in a few-layer graphene sample. IR spectroscopy typically is useful for studying the symmetry of the optical phonon modes.

When a particular phonon amplitude has the same symmetry as a vector, the corresponding phonon can directly absorb (or emit) a photon. Such phonon modes are called IR-active phonon modes. If the unit cell of a solid (or a molecule) has inversion symmetry, then the phonon modes can further be classified as either even and odd functions of the inversion operator, corresponding to Raman and IR-active phonon modes, respectively.[13] Thus, by using polarized IR absorption spectroscopy for such materials, we can get independent information on the symmetry of specific phonons. For example, achiral nanotubes (armchair or zigzag nanotubes) have inversion symmetry along the nanotube axis. Since carbon materials tend to absorb light readily, IR absorption is typically measured by using reflected light in the back-scattered geometry. Complementary IR and Raman studies on sp^2 carbon materials have been performed [159,160] and used to study the symmetry of specific phonons in these materials.

2.3.6. *Coherent phonon spectroscopy*

In this section, we first describe the generation and measurement of coherent phonons (CPs) in general and then illustrate the use of this measurement technique in the case of carbon nanotubes [45,161–165]. When the duration of a light pulse is of the order of 10 fs which is smaller than the period of vibrational modes, then atomic vibrations start at the same time as the el–ph interaction starts to act on all involved atoms. This means that the amplitude of each phonon vibration has the same phase for all atoms, and we call this effect the coherent motion of a vibration. When we now send a second light pulse, we can then observe the vibrations of the atoms by a time-dependent transparency of the light, for which the mean frequency values correspond to the experimentally determined phonon frequencies. When we make a Fourier transform of the time-dependent transparency of materials, sharp peaks appear at the frequencies of the phonon modes which have strong el–ph matrix elements. The observed results are then similar to those obtained in Raman spectra. From the observation of the phase of the time-dependent transparency vibration, we can obtain information on the coupling constant of the el–ph interaction. For example, in the case of nanotubes, the nanotube can start a RBM phonon vibration by either increasing or decreasing its diameter, depending on the mod$(2n + m, 3)$ type of the nanotube. With ultra-fast laser spectroscopy, it is possible to monitor the photo-induced electronic and vibrational dynamics on a femto-second timescale. In general, time-domain observations of the phonon dynamics require the generation of CPs, corresponding to in-phase lattice vibrations of an ensemble of the same species that add up constructively to generate a detectable signal [45,161,164,165]. CPs have been

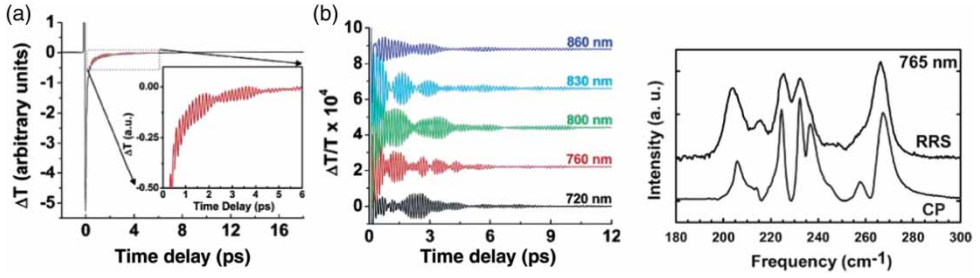

Figure 16. (a) Pump–probe time-delay data taken on a nanotube sample at a central wavelength of 800 nm in (b). The decay of the pump–probe signal within several picoseconds reflects the decay of the excited-state population. The inset in (a) is a zoom-in of the data between 0.3 and 6 ps, highlighting the coherent phonon contribution to the signal. (b) CP oscillations excited and measured at five different E_{laser} excitations (expressed in terms of their wavelengths). The individual traces for each wavelength are offset for clarity. The slower decay of the excited-state population has been subtracted in each case. (c) Phonon spectrum detected at a center wavelength of 765 nm obtained from both resonant Raman scattering (RRS) and from CP measurements in the frequency range of the RBM [45]. Adapted from carbon Nanotubes: Advanced Topics in the Synthesis, Structure, Properties and Applications, A. Hartschuh [45]. Copyright (2008) from Springer.

observed in a variety of different systems including thin films, semiconducting nanostructures, fullerenes and other carbon nanostructures.

Figure 16 shows results from coherent oscillations of the RBM coordinate, namely the diameter of the nanotubes [45]. Upon short-pulse laser excitation, all nanotubes of a certain (n, m) species within the sample will breathe in phase. By Fourier transforming this signal, the resulting response is similar to what is obtained in the frequency domain of resonance Raman spectroscopy. Upon close examination, however, noticeable differences are observed between CP and resonance Raman spectroscopy (RRS) data that were obtained from the same sample. For example, the spectral width of the phonon bands in the CP spectra is sharper, while the chirality dependencies of the CP and RRS signal intensities are different. Namely, in Raman scattering, the signal strength decreases as $(2n + m)$ increases, whereas the CP signal increases with increasing $(2n + m)$. These different types of behaviors can be used to distinguish one type of mechanism from the other in fast optics studies. Furthermore, pump–probe coherent phonon experiments on nanotubes (such as in Figure 16) also are very useful for finding the lifetime of photo-excited electrons in excited states.

2.4. *Raman spectroscopy of sp^2 carbons*

In this section, a brief introduction to Raman spectroscopy in sp^2 carbons is presented, starting with some historical background and then very briefly mentioning a number of different types of Raman spectroscopy that are being used to study sp^2 carbon materials.

2.4.1. *Historical background*

Raman spectroscopy has historically played an important role in the study and characterization of sp^2 carbon materials [19,166,167], which are being widely used in the last four decades to characterize pyrolytic graphite, carbon fibers [19], glassy carbon, pitch-based graphitic foams [101,168], nanographite ribbons [59], fullerenes [23], carbon nanotubes [32,167] and graphene [5,97,112]. For sp^2 nanocarbons, Raman spectroscopy can give information about crystalline size, clustering of the sp^2 phase within a given sample, the presence of sp^3 hybridization and chemical impurities, its mass density, optical energy gap, elastic constants, doping, defects and

other crystal disorder, edge structure, strain, the number of graphene layers, nanotube diameter, nanotube chirality and nanotube metallic vs. semiconductor behavior [169]. Another important area where much work has been done is on disordered, amorphous and diamond-like carbons [19,131,169], as well as graphite and graphene edges [151,170].

2.4.2. *Raman spectra of graphite and graphene: G- and G′-bands*

Figure 4 shows the Raman spectra from different crystalline and disordered sp^2 carbon nanostructures and emphasizes the difference in these spectra from one sp^2 carbon material to another. The first spectrum shown is that for mono-layer graphene – the building block of many sp^2 nanocarbons. A clear message derived from Figure 4 is that every different sp^2 carbon material in this figure shows a distinct Raman spectrum, which can be used to understand the different properties that accompany each of these different sp^2 carbon structures. For example, 3D highly oriented pyrolytic graphite (labeled HOPG in Figure 4) shows a distinctly different spectrum from that of mono-layer graphene (1-LG), which in turn is distinct from the Raman spectra characteristic of the various few layer-graphene materials, such as for 2-LG and 3-LG (see sect. 4.2) [112].

2.4.3. *First-order RBM, G^+ and G^- Raman spectra of SWNTs*

The Raman spectrum for SWNTs is also shown in Figure 4. These spectra show a variety of features, such as the RBM and the splitting of the G-band into G^+ and G^- bands. These first-order Raman features distinguish a SWNT from all other sp^2 carbon nanostructures. Carbon nanotubes are unique materials in many ways. For example, SWNTs exhibit transport properties that are either metallic (where their valence band and conduction bands touch each other at the K and K' points in the graphene BZ) or semiconducting (where a band gap, typically of several hundred meV, separates their valence and conduction bands). The Raman G^- spectral feature differs in lineshape, linewidth and frequency, according to whether the resonant nanotubes are semiconducting or metallic, as shown in Figure 17 [171] regarding their G^- and G^+ frequencies.

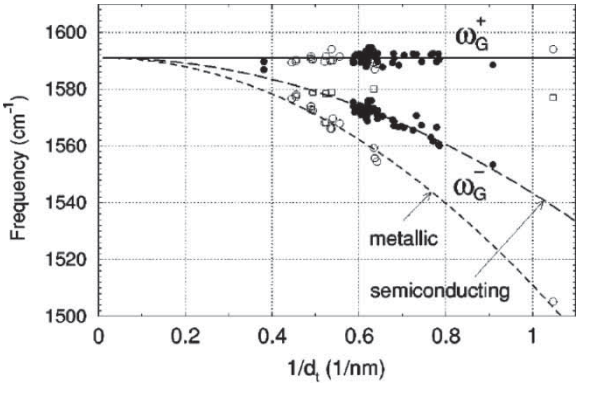

Figure 17. ω_G^- and ω_G^+ for semiconducting (filled circles) and metallic (open circles) SWNTs are plotted as a function of $1/d_t$. The flat solid line shows $\omega_G^+ = 1591\,\mathrm{cm}^{-1}$. The curves are given by the function $\omega_G^- = 1591 - C/d_t^2$, where $C = C_S = 47.7\,\mathrm{cm}^{-1}\mathrm{nm}^2$ for semiconducting SWNTs (long dashed curve) and $C = C_M = 79.5\,\mathrm{cm}^{-1}\mathrm{nm}^2$ for metallic SWNTs (short dashed curve). Also plotted (open squares) are the data for the $\sim 1580\,\mathrm{cm}^{-1}$ Lorentzian peak sometimes observed in metallic SWNTs. Adapted with permission from A. Jorio *et al.*, Physical Review B 65, p. 75414, 2001 [171]. Copyright © (2001) by the American Physical Society.

2.4.4. *The defect-induced Raman spectral features: D- and D′-bands*

The introduction of disorder breaks the crystal symmetry of graphene, 3D graphite and carbon nanotubes. The presence of disorder activates certain vibrational modes that would otherwise be silent, such as the D-band and the D′-band features and the combination D + *G* mode, shown in the spectrum-labeled damaged graphene in Figure [1,3,96,102,130,131,169,174]. The different types of defects do in fact show their own characteristic Raman spectra, as illustrated in Figure 4 by comparing the spectra-labeled damaged graphene and SWNH (denoting single wall carbon nanohorns, another nanostructured form of sp^2 carbon which may include pentagons with a small content of sp^3 bonding [37]). The topic of distinguishing between the Raman spectra of one and another type of defective sp^2 carbon remains an area for future study. When the disorder is so dominant that only nearest-neighbor structural correlations are present (labeled amorphous carbon in Figure 4), broad one-phonon ($<1600\ cm^{-1}$) and two-phonon (1600–3200 cm^{-1}) Raman features are seen [3,130]. At larger disorder limits, both sp^2 and sp^3 bonding might be seen. Some hydrogen uptake can also occur for such materials to satisfy their dangling bonds [131].

2.5. *Laser Raman scattering measurements*

In this section, we discuss the various types of Raman scattering studies that are generally carried out and we briefly describe in more detail how the measurements are done and the information that is provided by these measurements.

2.5.1. *The Raman setup*

In order to get a sharp and strong Raman signal, we generally use a laser light source. In the back-scattering geometry, the scattered light is collected at the same side of the laser spectrum relative to the position of the sample. Typical observation times to collect the scattered photons are from 1 s to 10 min. The incident and Rayleigh scattered light is filtered from the scattered light by a notch filter or some other method. The frequency shift of the Raman scattered light is measured by a monochromator which splits the observed scattered light as a function of the shift in the wavenumber of the scattered light relative to that of the incident light. The Raman intensity of each spectral line is measured by counting the number of photons recorded for that line and by considering the instrument function of the monochromator and the CCD detector to get a properly calibrated Raman signal. A typical resolution of a high-quality Raman system is $1\ cm^{-1}$. Splittings of the Raman spectra caused by experimental perturbations (such as due to external fields or applied stress) are directly measured by a CCD camera which counts photons, measuring frequency shifts, intensities and lineshapes of each pertinent Raman line.

2.5.2. *Polarized and micro Raman measurements*

Polarization is used to get additional information about crystal symmetry and selection rules. Symmetry information can be obtained by changing the polarization of the electric field of the light through use of suitable polarizers. The polarized incident light beam is focused on the sample and the scattered light is filtered by one polarizer and detected by a second polarizer. By selecting the propagating direction of the incident and the scattering light relative to the aligned sample and by selecting the polarization angles of the incident and scattering light beams, the optical dipole selection rules can be studied. This is the most common method that is used to determine the symmetry of the relevant phonons.

Micro Raman spectroscopy is a measurement technique in which the laser light of a given wavelength (or photon energy) is focused on the sample by an optical microscope. Such a system

is called a micro-Raman set up since the spatial resolution of the Raman signal is of the order of one micron. Not only is the incident light focused on the sample, but also the scattered light is collected by the same optical lens and is split by a half mirror [173]. An isolated graphene flake or SWNT on a Si substrate is located by putting the substrate on a mobile stage that moves the sample horizontally, and the mobile stage is controlled by stepping motors.

2.5.3. *Confocal Raman spectroscopy and Raman imaging*

Confocal Raman spectroscopy makes use of spatial filtering by means of pinholes in the optical paths, and it can generate spatially resolved Raman emission with a resolution on the order of $\lambda_{laser}/2\,\mathrm{m}$, where λ_{laser} is the laser wavelength. By scanning the substrate on which an isolated nanotube or a graphene sample is located, we can get a Raman signal as a function of the position on the sample, which is generally called Raman imaging (see Figure 18). In the case of nanotubes, a micro-Raman imaging scan of a substrate can find the location of the nanotubes resonant with a given laser line. If we instead use near-field spectroscopy (see Sections 2.6.3 and 2.6.4), we can even get information on the Raman signal as a function of the position of an individual isolated nanotube with a resolution on the order of 10 to 20 nm. In the case of graphene or graphite, the D-band imaging technique is also important for determining the distribution and specific location of defects over the sample, since the D-band feature is not symmetry allowed, but is instead induced by a symmetry-breaking mechanism such as a defect or an edge [174].

2.5.4. *Characterization of the sample edges and the imaging of defects*

Since the D-band in sp^2 carbons is a feature that is only observed when the crystal symmetry is broken by a defect or a sample boundary, the D-band intensity can be used to characterize the disorder in graphene and carbon nanotubes. This effect is clearly observed in Figure 18 which shows two confocal Raman images of a $6\,\mu\mathrm{m}$ highly oriented pyrolytic graphite crystallite deposited on a glass substrate. Figure 18(a) shows a Raman image of the crystalline regions of the sample, obtained by plotting the spatial dependence of the G-band intensity. In Figure 18(b) a map of the intensity of the disorder-induced D-band is shown, while Figure 18(c) shows two Raman spectra, one taken at the interior location of the crystalline region, and the other is taken at the edge. It is clear from Figure 18(a–c) that the G-band intensity is uniform over the whole graphite surface, while the D-band intensity is localized where the crystalline structure is not perfect, which

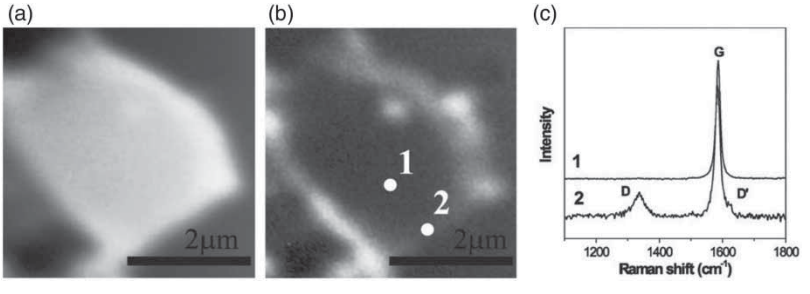

Figure 18. Raman spectra imaging of an HOPG micro-crystallite. In (a) the G-band intensity is plotted. In (b) the D-band intensity is plotted. (c) Spectra 1 and 2 are the spectra at locations 1 and 2 in (b) [174]. This experiment was performed in the laboratory of Prof. Achim Hartschuh and represent, to our knowledge, the first Raman imaging of localized defect modes in graphitic materials. M.A. Pimenta *et al.*, Physical Chemistry Chemical Physics 9, pp.1276–1290, 2007 [174]. Reprinted by permission of the PCCP Owner Societies.

occurs mainly at the edges of the crystalline region where symmetry-breaking occurs and D-band intensity due to the edge discontinuity is also seen.

The intensity of the D-band can also be used to assign the atomic structure of the edge in graphite and graphene [170], so that it can provide a useful tool to probe the edge chirality of graphene. In particular, armchair edges have a large matrix element for D-band scattering while for zigzag edges the matrix element for D-band scattering should vanish, and chiral edges show an intermediate amount of D-band edge scattering. However, imperfect graphene edges produced by the mechanical cleavage of graphite can produce ambiguous results that do not clearly discriminate the armchair and zigzag edges from one another.

2.5.5. *Resonance Raman spectroscopy*

In the Raman measurement, the resonance Raman effect strongly enhances the Raman intensity when the energy of either the incident or the scattered light matches the optical transition energy of a carbon nanotube or of a graphene ribbon. In the case of carbon nanotubes, since the JDOS becomes singular for an excitonic transition, the resonance Raman effect is especially strong. This is a major reason why we can get a strong Raman signal even from one nanotube [111]. On the other hand, if the resonance condition is not satisfied, we cannot get a measurable Raman signal even if a nanotube intersects with the light beam. This situation makes the search for isolated nanotubes in a sample very time consuming. Here, Rayleigh scattering is helpful for locating an individual SWNT and in providing its (n, m) assignment because all the nanotubes in a sample can thus be identified. However, with Raman spectroscopy we can always get a resonance Raman signal for bundle samples, but in this case we see only those nanotubes that are in resonance with E_{laser}. In the case of graphene which is a 2D system, the DOS is continuous near the Fermi energy and is not singular, so that any laser energy satisfies the condition for observing Raman spectra.

2.5.6. *The Raman excitation profile*

Using a continuous laser excitation energy light source, the Raman excitation profile (or resonance window) of a carbon nanotube is a plot of the Raman intensity measured at the same location on a sample as a function of laser energy. To determine the resonance energies of a carbon nanotube, denoted by E_{ii}, it is necessary to find the frequency of the peak in the Raman spectra taken as a function of the laser excitation frequency (E_{laser}), as shown in Figure 19(a). The FWHM intensity of the Raman excitation profile is defined as the resonance window width (typically 10 meV) which is inversely proportional to the lifetime of the photo-excited carriers (0.1 ps). The lifetime is defined as the time for the photo-excited electron to emit a phonon when it is in the excited state. In the case of the G-band, when we scan the laser excitation energy we can see two peaks satisfying the incoming and outgoing resonance conditions for the incident and the scattered light, while in the case of the RBM the two peaks for the incident and scattered light normally overlap with each other, since the resonance window width is larger than the RBM energy.

2.5.7. *The Kataura plot*

From the E_{ii} energy measured by the Raman excitation profile, we can plot E_{ii} for each (n, m) SWNTs as a function of the SWNT diameter, which we call the Kataura plot (Figure 19(b)) [176,177]. From the Kataura plot, we can determine the resonance conditions for all (n, m) SWNTs which is useful for assigning the (n, m) value to specific SWNTs from actual Raman measurements [178]. Since the radial breathing mode frequency ω_{RBM} depends on the SWNT diameter [111], we can plot the E_{ii} energy which is obtained by the resonance Raman excitation profile as a function of

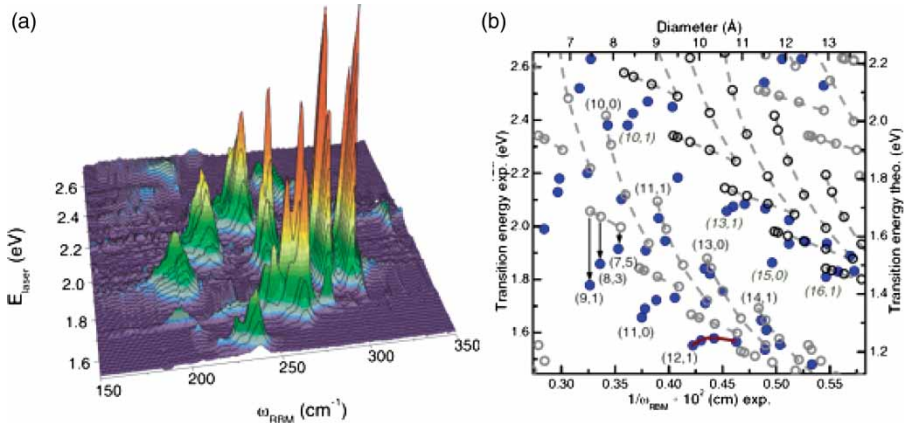

Figure 19. (a) RBM Raman measurements of HiPCO SWNTs dispersed in an SDS aqueous solution [152], measured with 76 different laser lines E_{laser} [175]. The non-resonance Raman spectrum from a separated CCl_4 solution is acquired after each RBM measurement, and this spectrum is used to calibrate the spectral intensities of each nanotube and to check its frequency calibration. (b) Filled circles are experimental E_{ii} vs. ω_{RBM} data points obtained by Telg *et al.* [107] from analysis of an experiment very similar to the one shown in (a). The label "Transition energy exp" actually indicates the excitation laser energy (E_{laser}) for each data point. Open circles come from third-neighbor tight-binding calculations, showing that even the addition of interactions with more neighbors in the π-band based tight-binding model is not enough to accurately describe the experimental results. Gray and black circles indicate the calculated optical transition energies from semiconducting (E_{22}^S and E_{33}^S) and from metallic (E_{11}^M) tubes, respectively. (a) Adapted from M.J. O'Connell *et al.*, Science, 297, p. 593, 2002 [152]. with permission from AAAS. And adapted with permission from C. Fatini *et al.*, Physical Review Letters 93, p. 147406, 2005 [175]. Copyright © (2005) by the American Physical Society. (b) Reprinted with permission from H. Telg, *et al.*, Physical Review Letters 93, p. 177401, 2004 [107]. Copyright © (2004) by the American Physical Society.

ω_{RBM}, and we call this plot an experimental Kataura plot. Figure 19(a) shows a 2D RBM map for the HiPCO nanotube sample in aqueous solution wrapped by the SDS (sodium dodecyl sulfate) surfactant [175]. For the construction of the plot in Figure 19(a), 76 different laser lines were used. By fitting each of the spectra with Lorentzians, (n, m) indices were assigned to the different SWNTs. Solid circles in Figure 19(b) denote the E_{ii} values obtained experimentally by fitting the resonance windows extracted from similar data to that shown in Figure 19(a), as compared with the E_{ii} obtained from tight-binding calculations (open circles) shown in Figure 19(b) [107].

2.6. *Other measurement techniques related to Raman spectroscopy*

In this section, we briefly describe several experimental techniques that have grown out of Raman spectroscopy or are related to Raman spectroscopy and are sensitively employed for specific types of optical studies used to gain unique and detailed information about nanostructures.

2.6.1. *Surface-enhanced Raman spectroscopy*

When light is incident on a small (nm in diameter) metallic particle, such as a gold or silver particle, the electric field near the metallic nano-particle is enhanced by several orders of magnitude, due to the surface plasmon excitation of the particle. The enhancement of the electric field

near the metallic nano-particle is given by the boundary condition for the transmitted electromagnetic wave on the metallic surface. When the light beam on the sample is located at the metallic nano-particle, the corresponding Raman signal becomes significantly enhanced (sometimes up to 10^{10} times that of the normal Raman signal). The surface-enhanced Raman spectroscopy (SERS) technique was utilized initially to obtain a large enough signal to observe the spectra from an isolated individual SWNT [128,179–181]. Changes in the symmetry selection rules are observed due to local symmetry breaking [182]. SERS measurements were carried out on SWNTs before researchers realized that there was a strong resonance effect occurring in the π-related states in carbon nanotubes and that this resonant effect was large enough to generate a measurable signal, without any SERS enhancement effect. In fact the observation of strong SERS spectra stimulated the first effort to observe the spectrum from one individual carbon nanotube [111]. Recently, the use of the SERS technique has been applied to graphene [183–186].

2.6.2. *Surface and interference enhanced Raman spectroscopy*

When we place a multi-layered sample on the top of a substrate, we can enhance the electric field of the light at the substrate by the interference of the incident light and the multi-reflecting light. This technique is called interference enhanced Raman spectroscopy and this technique can be used to get a large Raman signal from a graphene or a graphene nano-ribbon sample. Interference-enhanced Raman spectroscopy can also be combined with SERS and RRS, in which case the effect is called surface and interference co-enhanced Raman spectroscopy (SICERS) [184,187].

2.6.3. *Near-field enhanced Raman spectroscopy*

In order to get higher spatial resolution, an apex with a small aperture and a sharp tip at the end of an optical fiber is used to focus the light [45,188]. Since the diameter of the small aperture is smaller than the wavelength of the light, the light cannot get out from the aperture as a electromagnetic wave, but instead emerges as an exponentially decaying electric field which follows from a solution to Maxwell's equations. This decaying electric field of the light is called the near field while the conventional electromagnetic wave is called the far field. The amplitude of the near field can be much larger than that of the far field, and thus if the optical set up is sufficiently close to the sample, then we can get a much stronger signal with high spatial resolution using the near-field Raman technique, especially when tip enhancement techniques are used (Section 2.6.4). As discussed above, confocal Raman spectroscopy exhibits a limited resolution due to the Rayleigh criterion where the light cannot be spatially focused to better than $\sim \lambda/2$. This limitation can be overcome using near-field optical spectroscopy. We elaborate on this technique below in discussing the enhancement produced by using a metal tip and then by applying a combination of near field Raman and photoluminescence imaging to enhance atomic force microscopy imaging.

2.6.4. *Tip enhanced Raman spectroscopy*

Recently, laser-illuminated metal probes have largely been utilized to locally enhance electromagnetic fields, thereby generating a near-field effect [45]. So far, this so-called tip-enhanced microscopy (TERS, in comparison with more usual surface-enhanced techniques) has been applied to both Raman scattering and photoluminescence studies of SWNTs, and it is based on the local field enhancement at a laser-illuminated metal probe (see Figure 20). The highest spatial resolution achieved up to now is about 10 nm, which is limited by the tip size [45]. Near-field optical microscopy also provides significant signal enhancement by several orders of magnitude, which is crucial for efficient nanotube and graphene ribbon detection. The combination of nanoscale resolution and signal amplification makes the near-field optical techniques ideally suited

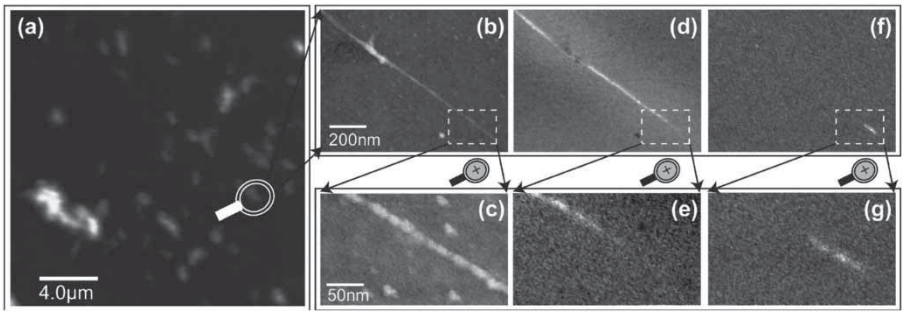

Figure 20. Imaging of DNA-wrapped SWNTs at different magnifications: (a) A confocal Raman image of a DNA-wrapped SWNT using an excitation wavelength of 632.8 nm. Topographic images in (b) and (c) indicate a periodic height modulation expected for wrapping with short DNA segments. Near-field Raman images (d) and (e) show the G-band intensity around 700 nm, and in (f) and (g) the intensity of photoluminescence images at around 950 nm corresponding to the emission wavelength of an (8,3) nanotube are shown. PL occurs only in the lower section of the nanotube where the Raman intensity is significantly weaker. The abrupt transition from strong to weak Raman scattering combined with the appearance of PL is interpreted as a local change in the nanotube (n,m) chirality [45]. Here, we see the power of near-field spectroscopy to show images with spectroscopic information at high spatial resolution. Adapted from carbon Nanotubes: Advanced Topics in the Synthesis, Structure, Properties and Applications, A. Hartschuh [45]. Copyright (2008) from Springer.

for the investigation of nano-materials or localized perturbations caused by defects or nonuniform environments. The use of the TERS technique is time consuming and requires great care in its execution.

2.6.5. *Simultaneous atomic force microscopy, near-field Raman and PL imaging*

Figure 20 shows simultaneous near-field Raman and photoluminescence (PL) imaging for SWNTs grown on glass by the arc discharge method [45], where highly confined PL imaging from short 20 nm long segments of about 20 nm in length has been observed from SWNTs. The PL from micelle-encapsulated SWNTs on mica typically comes from much longer (more than 100 nm long) SWNT segments of up to several hundreds of nanometers. Figure 20 shows PL emission in images coming from a DNA-wrapped nanotube at different magnifications, starting with about 75 nm in the lower part of the nanotube (Figure 20g). The intensity of the Raman signal is seen to decrease sharply at the position where PL starts to occur and the results obtained in this particular image indicate a change in nanotube chirality (Figure 20e).

2.6.6. *Coherent anti-Stokes Raman spectroscopy (CARS)*

The CARS technique [189,190] consists of a pump–probe experiment using laser light. The electrons in the ground state are excited by the pump laser light and the electron excitation is transferred to a phonon via a Stokes Raman process. Then by the second probe light pulse, the phonon excitation is transferred to another electron by an anti-Stokes Raman process. In this subsequent process, we can observe the anti-Stokes Raman signal. An important concept in CARS is the coherence of the Raman processes. Since the amplitude of the anti-Stokes Raman scattered light has the same phase as the pump laser light, the CARS amplitude (intensity) is proportional to the square of the number of molecules or atoms in the sample. In order to obtain this coherence, a non-resonance condition is selected for both the first Stokes and the second anti-Stokes processes.

Since CARS observes a blue-shifted signal, the signal is well separated from the related red-shifted photoluminescence signal.

2.7. *Kohn anomaly in graphene and carbon nanotubes*

The use of the gate voltage to vary the electrochemical potential of a nanostructure has provided a very sensitive tool to probe many different phenomena that are sensitive to the carrier density, such as the Kohn anomaly (KA) [127,191–194]. We discuss the dependence of the Kohn anomaly on the frequency and linewidth of the G-band phonon for mono-layer graphene in Section 2.7.1, and for bi-layer graphene in Section 2.7.2, and for metallic SWNTs in Section 2.7.3. A theoretical approach to the KA of carbon nanotubes is later discussed in Section 3.6.5 and 5.4.4.

2.7.1. *Kohn-anomaly of the G-band of graphene*

In Figure 21, the G-band Raman spectra of graphene is shown as a function of applying a gate voltage to the substrate on which the graphene sample is positioned [195]. Here, the G-band is observed to upshift in frequency with both negative and positive applied potentials (see Figure 21(a) and (b)) and this frequency upshift is accompanied by a decrease in its linewidth (see Figure 21(c)) which is observed for both electron or hole doping. These effects are known as the Kohn anomaly [194,196–199]. These observations are explained as follows.

In the presence of the el–ph interaction of free electrons near the Fermi energy E_F, the phonon frequency and spectra become, respectively, down-shifted and broad, which is given by second-order, time-independent perturbation theory for the phonon energy and the phonon self-energy [194,196–199]. When the Fermi energy shifts from the Dirac point by more than 0.1 eV ($\pm\hbar\omega_G/2$), the virtual absorption of an electron by a G-band phonon with an energy of 0.2 eV is suppressed and thus a phonon hardening occurs. Furthermore, since the el–ph interaction is suppressed, the lifetime of a phonon becomes large, which corresponds to the decrease in linewidth shown in Figure 21(c).

2.7.2. *Kohn anomaly of bi-layer graphene*

In bi-layer graphene, the unit cell has four C atoms rather than two, and as a result there are two π bands and two π^* bands at the K point. In this case, there will be more than two Kohn anomalies in the G-band gate-dependent frequency renormalization [200]. When the Fermi energy reaches $\pm\hbar\omega_G/2$, the π–π^* transition from the valence band to the lower conduction band shown in Figure 22(I) is no longer allowed, as it is in mono-layer graphene. However, the transition from the now filled lowest energy π^* band to the higher energy π^* band, shown by the dashed arrow in Figure 22(II), is possible. Therefore, when the gate voltage rises further and the Fermi energy reaches the second band, then the π^*–π^* transitions shown in Figure 22(III) are suppressed. These effects are seen in the G-band frequency and linewidth of bi-layer graphene (see Figure 22)[191, 200], where a distinctly different behavior with respect to the mono-layer case (see Figure 21) is clearly observed for both the G-band frequency and linewidth.

Furthermore the interlayer interaction between phonons in bi-layer graphene gives rise to even and odd functions for the G-band vibrational modes in which only the even function mode is Raman active. However, if an interaction with the substrate exists, this symmetry-imposed effect is relaxed and both even and odd types of G-band spectra can be observed [5].

2.7.3. *Kohn anomalies of SWNTs*

Similar Kohn anomalies of the G-band for SWNTs when compared with mono-layer graphene are observed [193], but for SWNTs there is also a dependence on both the diameter and chiral angle [196,199,201–203]. In this case, the RBM mode also shows a weak phonon softening effect [170,204,205], which is further discussed in Section 5.

The Raman spectra of the G-band of sp^2 carbons have an asymmetric lineshape if there are free electrons at the Fermi energy. The asymmetric lineshape is expressed by Breit–Wigner–Fano lineshapes (BWF), whose origin is generally understood by an interference of discrete energy levels with a continuum energy spectrum (Fano resonance [129]). The second-order perturbation theory expression for the el–ph interaction for the KA only gives a symmetric broadening of the phonon spectra and thus the el–ph interaction by itself is not sufficient to account for the observed BWF lineshapes. There is, however, another continuum spectra for the electron excitations involving the Coulomb interaction in which there is an electron–electron interaction between photo-excited electrons and the free electrons associated with the SWNTs that is relevant to accounting for the BWF lineshapes. Recent measurements of the electronic Raman spectra of SWNTs clearly show a BWF asymmetric shape depending on the energy position of E_{ii} [202,206].

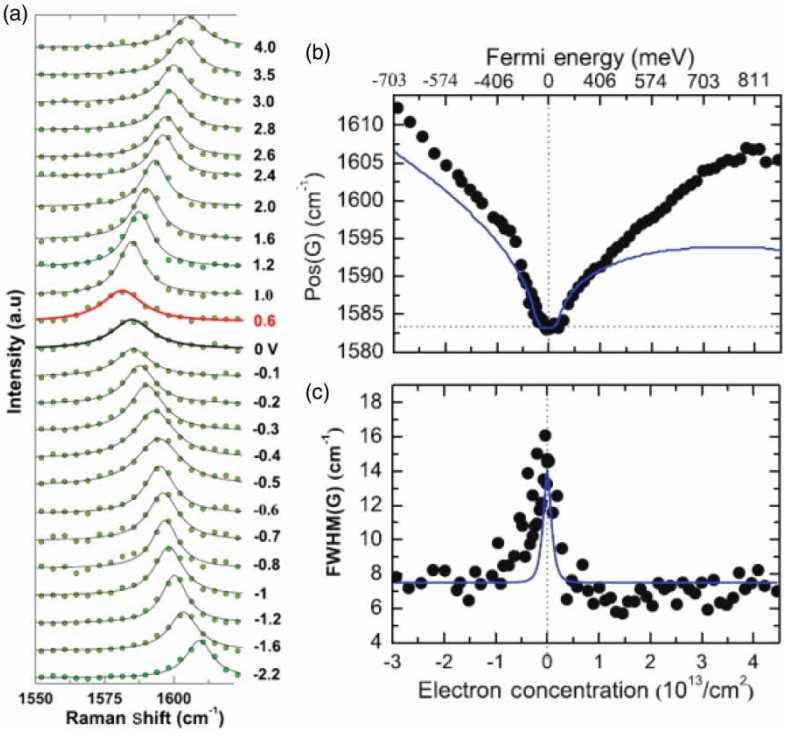

Figure 21. The dependence of the Raman G peak frequency of mono-layer graphene on doping using a gate voltage to provide positive and negative potentials. (A) The G-band spectra at 295 K for many values of the gate voltage V_g are shown. The darker line spectrum is at $V = 0$ but the spectrum at $V = 0.6$ V corresponds to the undoped case, which occurs at $V \neq 0$ due to the natural doping of graphene by the environment. (B) The G peak position (frequency) and (C) the G peak FWHM linewidth as a function of electron concentration as deduced from the applied gate voltage data are shown. Black circles show the measurements and the solid lines show results from a finite-temperature non-adiabatic calculation. Adapted with permission from Macmillan Publishes Ltd. Nature Nanotechnology [195], Copyright © (2008).

2.8. *Classification of Raman processes*

In this section, we classify the Raman spectra of sp^2 carbon materials from the point of view of Raman processes.

2.8.1. *First-order Raman process*

After photo-absorption, if one phonon is emitted by the el–ph interaction, we can observe the inelastically scattered light coming from the electron, whereby a phonon is emitted through the el–ph interaction in the first-order Raman spectra. Through the recombination of a photo-excited electron with the hole that was left behind, the scattered electron should have the same k value as the hole, which requires that the phonon q vector should be zero. The phonon thus produced is called a zone-centered (or a Γ point) phonon [104,207,208]. In the case of graphene, the degenerate LO and iTO phonon modes at the Γ point are Raman-active and are known as the E_{2g} symmetry phonon modes. These modes occur around 1585 cm^{-1}, while the oTO phonon mode occurs around 850 cm^{-1} and is an IR-active phonon mode, which does not contribute to the Raman spectra for either defect-free graphene or SWNTs. The remaining three modes are acoustic modes and have zero phonon energy at the Γ point. In the case of SWNTs, the RBM and G-band phonons correspond to first-order Raman processes.

2.8.2. *Two-phonon second-order Raman process*

After photo-absorption, if two-phonons are emitted by the el–ph interaction, then we can observe inelastically scattered light as a two-phonon second-order Raman process. In this case, there are two possibilities for the actual Raman processes. One process involves the harmonic formed by two

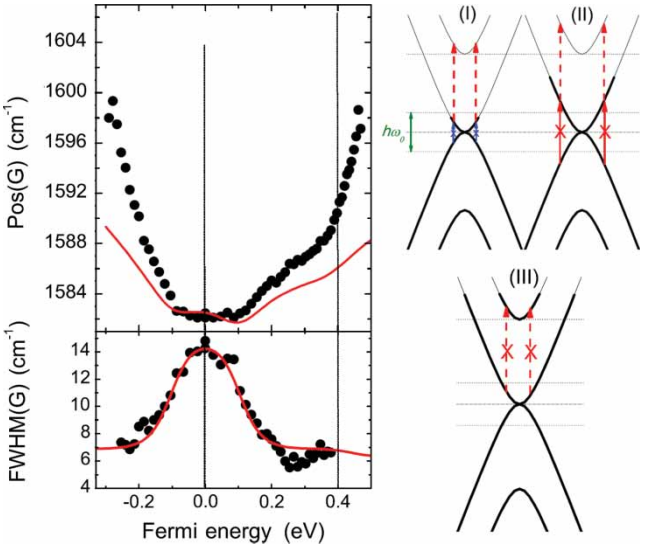

Figure 22. On the left, the peak frequency (Pos(G)) and linewidth (FWHM(G)) for the Raman G-band feature of doped bi-layer graphene vs. Fermi energy are shown. The black circles show the measurements and the solid line shows the finite-temperature non-adiabatic calculation. On the right, schematics of the el–ph coupling at three different doping levels, as indicated by the thicker lines on the electronic bands, are shown. Adapted figure with permission from A. Das *et al.*, Physical Review B 79, p. 155417, 2009 [191]. Copyright © (2009) by the American Physical Society.

Γ point phonons, which is an over-tone phonon mode and the overtone mode of the G-band appears at around 3170 cm^{-1} (twice the G-band mode frequency at 1585 cm^{-1}). A feature associated with the harmonic of the D′-band also appears at 3240 cm^{-1}.

The other process is given by emitting two K point phonons with q and $-q$ wavevectors by an inter-valley scattering process. By emitting two phonons with opposite q and $-q$ vectors, the photo-excited electron can go back to its original position and recombine with a hole. Because of the many possible $q \neq 0$ vectors, the spectral width for two-phonon Raman processes is broad compared with the linewidths typically found in the first-order Raman spectra. The G′-band around 2700 cm^{-1} arises from a two-phonon Raman process occurring near the K point iTO phonon mode. For both cases of two-phonon scattering processes, there is no restriction on $q = 0$ for either of these processes. Furthermore, the two phonons are not always the same types of phonon modes and can have the same wavevector but different frequencies. If two different phonon modes are involved in the two-phonon process, the Raman shift becomes the sum of the two phonon mode frequencies, which we call a combination mode. It is important to emphasize that combination modes which combine via an intra-valley scattering process together with an inter-valley scattering process are not possible since the corresponding q vectors would be completely different from each other[14] and conservation of momentum would be violated.

2.8.3. *One-phonon and one-elastic second-order Raman process*

In a real crystal lattice, there are many defect structures by which a photo-excited electron can be scattered by defects, such as the edges of graphene or point defects in both graphene and carbon nanotubes. As far as there is no elementary excitation creation or annihilation at the defect site, the scattering is elastic and only the momentum of the electron k can be changed to $k + q$ by the q component of the defect potential $V(q)$. There is also the possibility of a second-order Raman scattering process in which one of the two phonon scattering processes can be changed from an inelastic scattering process to an elastic scattering process. Here, we still call this scattering process a second-order Raman process, since the number of the order is defined by the number of scattering events that occur. For this process, the corresponding Raman shift involves only one phonon energy. What is different here from the first-order process is that the restriction on $q = 0$ is relaxed and many different phonon modes with $q \neq 0$ can contribute to the Raman spectra. The D-band around 1350 cm^{-1} is near the K point iTO phonon mode and the D-band intensity come from a Raman process involving one-phonon and one-elastic inter-valley scattering process. The D′-band around 1620 cm^{-1} is near the Γ point LO phonon mode which consists of one-phonon and one-elastic intra-valley scattering process. Since many q vectors are possible in this Raman process, defect-related Raman peaks are generally broad compared with typical first-order Raman features. The optical process which consists of only elastic scattering processes is the Rayleigh scattering process.

In Figure 23, we show the schematics for (a1,a2) first-order and (b1-b4) one-phonon second-order and finally (c1,c2) two-phonon second-order, resonance Raman spectral processes [209]. In Figure 23, we also show the incident and the scattered resonance conditions. For second-order Raman processes, a DR Raman condition is satisfied [104,209,210], which is clarified in Section 2.8.4. Although not shown in Figure 23, the Raman process for inter-valley phonons which connects the K and K' points in the BZ is a second-order process.

2.8.4. *Double resonance Raman spectra*

Referring to Figure 23 [104,208], there are three intermediate electronic states in second-order Raman processes: (1) excited states at k, (2) the intermediate state at $k + q$, and (3) the second